Neutrally stable tape spring actuation using shape memory alloys

Niels Groeneweg

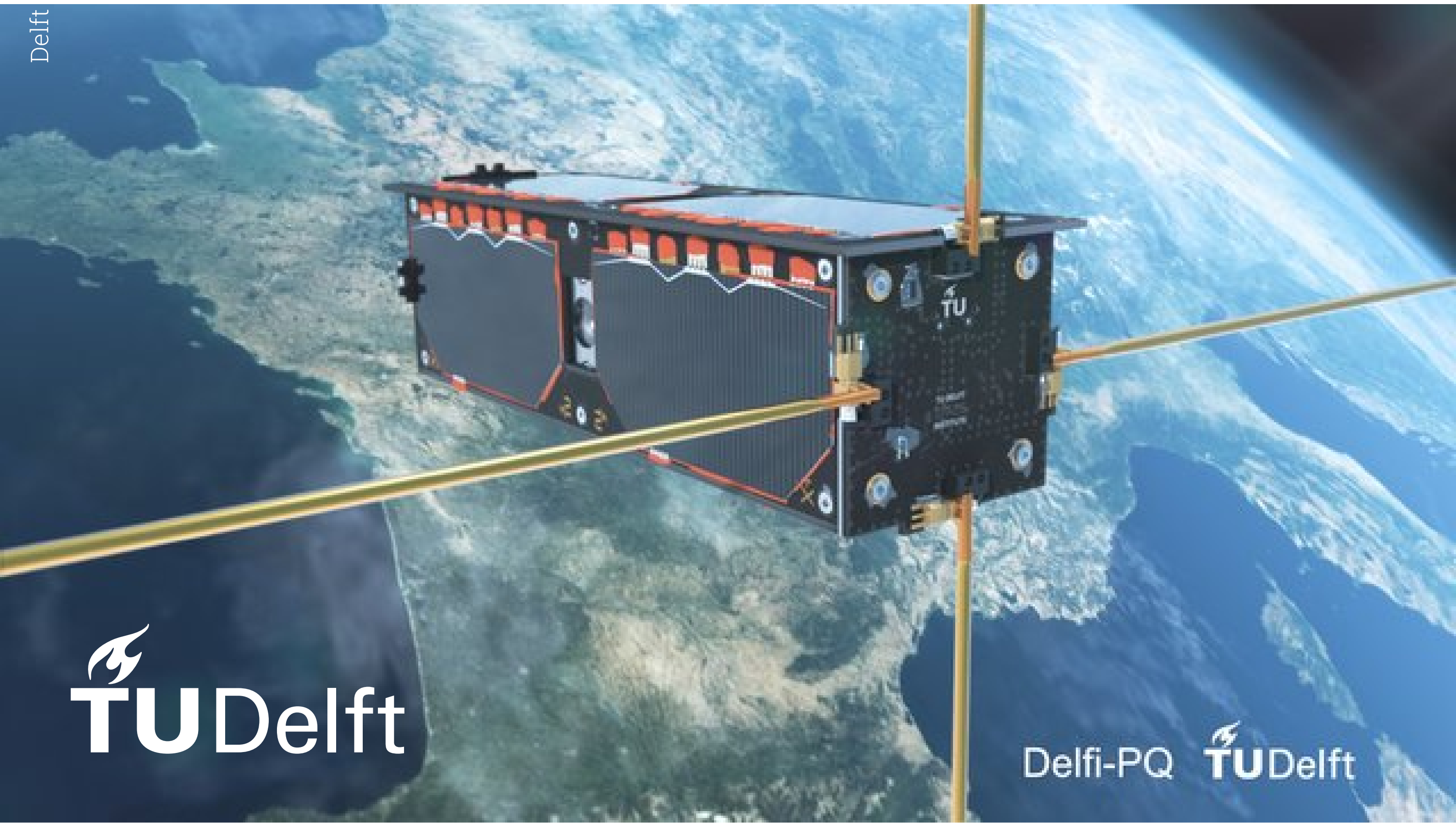

Neutrally stable tape spring actuation using shape memory alloys

by

Niels Groeneweg

to obtain the degree of Master of Science
at the Delft University of Technology,
to be defended publicly on Tuesday April 8, 2025 at 01:30 PM.

Student number:	4399080	
Project duration:	March 11, 2024 – March 25, 2025	
Thesis committee:	Dr. O.K. Bergsma,	TU Delft, chair
	Dr. J.A.M. Vanhamel,	TU Delft, examiner
	ir. I. Uriol Balbin,	TU Delft, thesis supervisor

Cover: DelfiPQ by TU Delft

An electronic version of this thesis is available at `http://repository.tudelft.nl/`.

TU Delft

Preface

This thesis project marks the end of quite a journey. After high school, I started my bachelor's in Aerospace Engineering, but found that I was out of my league. I spent four years at Hogeschool InHolland obtaining my bachelor's degree in Aeronautical Engineering, learning a lot of practical knowledge, developing as a person and doing some amazing internships. Still hungry for more, I decided to return to Aerospace Engineering to pursue the degree I still wanted. And now it is here. It was not always easy, but it has made me stronger and I am proud of myself for never giving up.

I would like to express my sincere gratitude to my supervisor Ines Uriol Balbin for being extremely helpful and patient throughout this project, and for being so interested in the topic and supportive of me working on it. I also particularly thank Otto Bergsma for the interesting discussions, Stefano Speretta and Sevket Uludag for their assistance from the Delfi team, and Victor Horbowiec and the other DASML staff for their support in the composites and instrumentation labs. Thank you also to everyone I have had the pleasure of working with on different projects and courses during this Master's program. Finally, thesis work would not be possible without support after hours, and I also thank my friends and family for providing me with a great environment to unwind in. I owe everyone above a debt of gratitude.

Niels Groeneweg
Delft, March 2025

Summary

Delft University operates a small satellite program called the Delfi family. For its upcoming satellite, Delfi-Twin, the Delfi team seeks an actuator capable of deploying an antenna. This actuator must support multiple stable configurations, extend an antenna of at least 36 cm in length, and potentially deploy additional appendages in the future. To achieve this, a specialized variant of a composite tape spring, known as the neutrally stable tape spring, was selected for investigation in this thesis. These tape springs actuate through a rolling motion.

Most tape springs are bi-stable, capable of maintaining both stowed and deployed positions. The rolling transition between these states can be violent, depending on internal strain energy levels, often necessitating the use of auxiliary control mechanisms. The neutrally stable tape spring, a relatively new concept introduced by Murphey & Pellegrino in 2004 and further developed by Schultz et al. in 2008, minimizes internal strain energy to near zero, enabling position changes with low-force actuators. In this thesis, shape memory alloys (SMAs) are used to generate these actuation forces. An SMA wire can be deformed into an arbitrary shape but returns to a predefined (typically straight) configuration when heated to a specific activation temperature, which can be achieved through electric current. The force exerted by the wire is related to its cross-sectional diameter.

The key to achieving neutral stability lies in using a composite matrix material with low shear stiffness, combined with $\pm$45-degree plain-weave plies. The composite used a 90 gsm plain-weave T300 fiber. In this Master's thesis, a resin mixture developed in a 2019 MSc thesis by Sebastien Callens was used, providing the necessary shear stiffness for successfully manufacturing neutrally stable tape springs in the DASML lab at the Faculty of Aerospace Engineering. A significant challenge encountered was the difficulty of producing tape springs at sufficiently small scales. While the Delfi team requested tape spring diameters of no more than 7 mm due to space constraints, manufacturing by hand proved challenging for diameters below 21 mm. Possible improvements in the manufacturing process may help alleviate this problem in the future.

Since the SMA component is activated at a specific temperature, a key focus of this thesis is analyzing the thermal conditions under which the tape spring will operate on Delfi-Twin. To determine these operating temperatures, thermal modeling was conducted using the ESATAN-TMS thermal modeling software. A simplified model of the future Delfi-Twin was developed and verified using known thermal sensor data from its predecessor satellite, Delfi-PQ. This analysis concluded that the SMA component should activate at temperatures no lower than 90°C. As a result, commercially available SMA wires under the trade name Flexinol were selected as the actuating component.

The required SMA wire diameter was estimated using a cantilever beam approximation for the tape spring, followed by testing with a laboratory setup. Three design configurations were evaluated: one integrating the SMA wire within the composite mid-plane of the tape spring, one positioning the wire on a spacer attached to the tape spring, and one utilizing a pair of parallel wires on the same spacer. The parallel-wire configuration proved to be the most effective, as it not only provided an electrical return path to the tape spring attachment point but also enhanced the actuation force without increasing the actuator's thickness.

While the tape spring's capability to deploy an appendage remains untested, it is expected to be feasible, provided that the SMA component generates sufficient force to bend both the antenna wire and the tape spring. This expectation is based on the fact that the wire is able to deploy the spacer component along with the tape spring. Additionally, the bending behavior could potentially be improved by employing an alternative matrix material with even lower shear stiffness. Further research is required to refine the detailed design of these SMA-actuated neutrally stable tape springs and to identify the optimal SMA component based on the specific satellite appendage to be deployed.

Contents

List of Figures

List of Tables

Nomenclature

Abbreviations

Abbreviation	Definition
AEW	Amine Equivalent Weight
CFRP	Carbon Fiber Reinforced Plastic
DASML	Delft Aerospace Structures and Materials Laboratory
EEW	Epoxy Equivalent Weight
ESATAN-TMS	ESATAN Thermal Modeling Software
FEM	Finite Element Method
IR	Infrared
MCRT	Monte Carlo Ray Tracing
PPH	Parts Per Hundred
SMA	Shape Memory Alloy
STEM	Storable Tubular Extensible Member
TS	Tape Spring
U	Unit, or 10x10x10 cm of volume in a CubeSat context

Symbols

Symbol	Definition	Unit(s)
A	Area	[m^2]
E	Young's modulus or tensile stiffness	[GPa, Pa]
F	Force	[N]
G	Grammage	[gsm]
G	Shear stiffness	[GPa, Pa]
I	Current	[A, mA]
I	Second Moment of Area	[m^4, mm^4]
L	Length	[km, m, cm, mm, ft, in]
M	Moment	[Nm]
m	Mass	[kg, g]
p	Power	[W]
U	Voltage	[V]
ν	Poisson's ratio	[-]

1 Introduction

In the last two decades, satellites have increasingly moved to smaller platforms [2]. In 1999, the CubeSat standard was introduced by Puig-Suari and Twiggs at the California Polytechnic State University, creating a standard satellite ”unit” of 10x10x10 cm or 1U. The standard aims to provide access to space for small companies and universities at a low cost. The concept proved to be a great success, with over 1400 satellites launched by the end of 2020. Other form factors followed soon after. In 2006, the lesser-known PCBSat was introduced, which is essentially a slice of a cubesat of 20 or 25 by 10x10 cm that runs off a single PCB. In 2009, Twiggs introduced an even smaller standard known as the PocketQube, which measures 5x5x5 cm. This provides an even smaller platform for simple space missions.

The focus of this thesis project is the Delfi series of satellites. This series started with the Delfi-C^3 (2008) and Delfi-n3xt (2013) cubesats. The project then moved to the PocketQube standard for its next generation satellite: the Delfi-PQ, launched in early 2022. The next step in this project will be to launch a pair or ”twin” of satellites, in order to test the concepts of formation flying and relative navigation for small satellites, as well as perform various measurements in low Earth orbit. This project has been given the name Delfi-Twin.

This thesis will focus on making a specific improvement based on the design of the Delfi-PQ PocketQube. This satellite holds four dipole antennas. These antennas are currently deployed through a spring and burn wire setup, which is a one-off and permanent deployment that moves the antenna from a stowed position to a locked and deployed position. A problem of this setup is that the antenna must be of roughly the same length as the satellite body since the antenna is fixed to a rotational joint at one end of the body and secured via burn wire at the other end. To allow more freedom in the design of the antenna, a new actuation mechanism is required that allows for the deployment of antennas that have a length that is independent of the length of the satellite body. For the purpose of this project, a placeholder antenna length of 36 cm is requested. For application on the satellite, the requested thickness of the actuator should be no more than 7 mm in order to fit between the satellite body and stowed solar panels. This poses a significant challenge.

Further wishes have been expressed for this new mechanism. The first is to allow for reversible operation of this mechanism such that the antenna can be stowed and deployed repeatedly. This will allow the antenna to be temporarily retracted in case of flights through the upper atmosphere and to manage the drag profile of the satellite. Secondly, it would be considered beneficial to future design efforts if the new mechanism is capable of actuating other satellite appendages. Within this project, a satellite appendage can be any kind of subsystem on a satellite that requires deployment before becoming fully operational. Examples can be antennas, which are the main focal point, but also solar arrays and radiators.

A literature study was conducted on various satellite appendage actuation mechanisms, from which tape springs were selected as a possible solution to the presented problem. A specific type of tape springs known as the neutrally stable tape spring, described by Murphey and Pellegrino [17] in 2004 and improved upon by Schultz et al [22] in 2008, is selected for further study. These tape springs hold low internal strain energy, allowing their manipulation by low-force actuating components such as shape memory alloys (SMAs) or piezoelectric films. In this thesis, SMAs will be used. Schultz et al specifically mention the possibility of actuating a neutrally stable tape spring in two directions, allowing for reversible deployment and stowage. The actuator presented by Schultz et al leads to the following research question:

How can an SMA-actuated neutrally stable tape spring be made viable for use as a deployment mechanism for small satellite appendages?

The research is split in four sub-questions, which focus on the design and manufacturing of the tape spring and that of the SMA component. Additionally, as the design is intended to be used in space, some study must be conducted on the thermal conditions in which the tape spring is expected to operate.

1. Which layup, fiber and epoxy combination constitute a suitable neutrally stable tape spring?
2. What temperature conditions must the tape spring withstand in space?
3. What are the manufacturing challenges in creating a neutrally stable tape spring?
4. How can a shape memory alloy component be effectively utilized as the actuating component of the tape spring?

A small set of initial requirements has been provided by the Delfi team. They are:

1. The actuator should be able to deploy an antenna, and if possible, other appendages in the future;
2. The preliminary antenna length is set to 36 cm;
3. The actuator should have multiple stable positions;
4. The maximum thickness of the actuator in the stowed configuration is 7 mm.

There is no hard mass requirement for the actuator. Given the design presented by Schultz et al it is expected that the tape springs will be lightweight (<10 g) relative to the satellite mass of approximately 750 grams.
Chapter 2 of this thesis provides a background in tape springs and shape memory alloys, which are the two components of the intended deployment mechanism. Chapter 3 focuses on the modeling of the satellite and tape spring using the ESATAN thermal modeling software with the intent of estimating the operational temperatures of the tape spring. Use is made of available temperature sensor data from the Delfi-PQ satellite as a way of model verification. Chapter 4 discusses the material selection process for the tape spring and SMA as well as the development of the tape spring manufacturing process. Use is made of carbon fiber and various epoxy resins, and experimental manufacturing is carried out in the DASML laboratory at the Faculty of Aerospace Engineering. Chapter 5 finally discusses a simple analytical cantilever beam model that is used to estimate the deployment of several spring designs. These predictions are tested in the instrumentation lab using a lab power source to heat and activate the SMA wires.

2

Tape Spring and Shape Memory Alloy Background

Tape springs are based on the concept of the Storable Tubular Extensible Member (STEM), which is essentially a type of spring. STEMs have been in use since the advent of spaceflight in the 1960's and were then made of metal. The first application of STEMs was on the Alouette satellites launched in 1962 and 1965, where STEMs were used as a deployable antenna [13]. The first of these antennas were made of steel and were 150 ft long, while a second generation was made of beryllium copper and measured 240 ft long. This change to a lighter material was made to reduce the antenna diameter and extend its length while maintaining the mass of the first satellite. Another application on a well-known satellite is on the Hubble space telescope, where the solar blankets on the satellite were deployed using a steel-made STEM variant known as the bi-STEM [5], which is a pair of STEMs that enclose each other.

The deployment concept of a STEM is based on the release of strain energy. This energy is generated by forcing the material in to a curved surface (Figure 2.2b) followed by heat treatment, which makes the curved shape a stress-free state. The STEM is then rolled up in to a flat shape, causing the material to store strain energy. Figure 2.1 shows the three states a section of spring can be in: the spring is either in its natural shape and stress-free, in a coiled shape and stressed due to being flattened when rolled, or in a transition shape between the two.

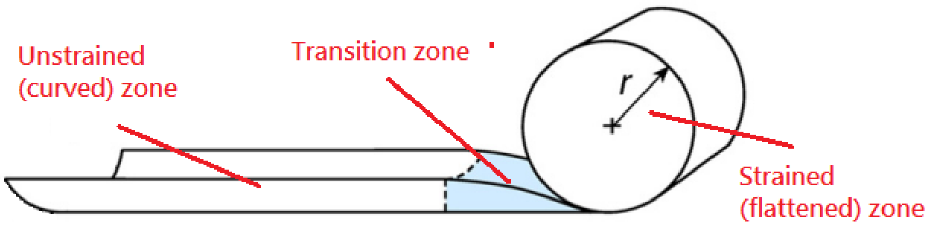

Figure 2.1: Strain zones in a STEM or tape spring

When unrolling of the STEM is initiated, the continuous release of the stored strain energy sustains the deploying movement of the entire spring. Because metals are isotropic materials, there is little control over the storage and release of strain energy. This uncontrolled deployment leads to shocks and overshoot movements which often require an auxiliary mechanism, such as a motor, to control.

Figure 2.2b shows the geometry of a tape spring. This geometry is characterized by the length L, thickness t, spanned angle α, and radius R. For a STEM, the spanned angle is typically large: close to 360 degrees or even larger, such that the spring folds in to itself and has a slit. For a composite tape spring, the angle is typically much smaller. The length of tape springs varies greatly. The 2017 InflateSail 3U cubesat used 2.3 m long tape springs to help in the deployment of a drag sail [29]. At the same time, NASA research has lead to the development of composite tape springs that are more than 15 meters long [18].

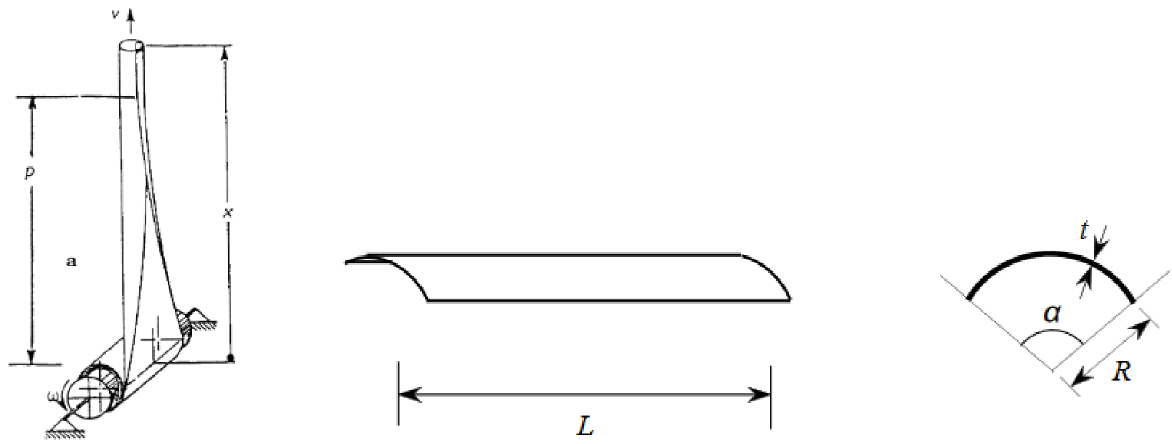

(a) Example of a STEM design

(b) Tape spring geometry

Figure 2.2: STEM and Tape Spring

The same NASA research also mentions two major advantages of composite tape springs: they can be up to 75% lighter and a hundred times less thermally expansive than thin-shell metallic booms. Composite materials enable more precise control over both the extent of strain energy storage and the rate of its release. These advantages contribute to a more controlled and predictable deployment process. A further introduction in to tape springs is provided in the following sub-chapters.

2.1. Bi-stable Tape Spring

Tape springs used on satellites are typically bi-stable. As the name implies, a bi-stable tape spring has two stable positions: the fully stowed and fully deployed positions. The fully deployed position has zero stored strain energy as the cross-section of the tape spring is in its curved, stress-free state, while the fully stowed position represents a second, non-zero, local minimum of strain energy. For a composite tape spring, the stored energy is dependent on the material as well as the geometry of the spring. Using classical laminate theory, an ABD-matrix can be created that describes the stress resultants in such a composite shell (Equation 2.1).

$$
\begin{bmatrix} N_x \\ N_y \\ N_{xy} \\ M_x \\ M_y \\ M_{xy} \end{bmatrix} = \begin{bmatrix} A & B \\ B & D \end{bmatrix} \begin{bmatrix} \epsilon_x \\ \epsilon_y \\ \gamma_{xy} \\ \kappa_x \\ \kappa_y \\ \kappa_{xy} \end{bmatrix} = \begin{bmatrix} A_{11} & A_{12} & A_{16} & B_{11} & B_{12} & B_{16} \\ A_{12} & A_{22} & A_{16} & B_{12} & B_{22} & B_{26} \\ A_{16} & A_{16} & A_{66} & B_{16} & B_{26} & B_{66} \\ B_{11} & B_{12} & B_{16} & D_{11} & D_{12} & D_{16} \\ B_{12} & B_{22} & B_{26} & D_{12} & D_{22} & D_{26} \\ B_{16} & B_{26} & B_{66} & D_{16} & D_{26} & D_{66} \end{bmatrix} \begin{bmatrix} \epsilon_x \\ \epsilon_y \\ \gamma_{xy} \\ \kappa_x \\ \kappa_y \\ \kappa_{xy} \end{bmatrix} \tag{2.1}
$$

In equation 2.1, the first vector describes the force and moment loads, the ABD matrix describes the mechanical properties of the composite part, and the last vector describes the strains and curvatures in the part. The exact values of the ABD matrix are found depending on the material properties of the matrix and fiber as well as the layup angles of the plies. According to Iqbal and Pellegrino [10], the total strain energy in a bi-stable tape spring is the sum of the internal bending and stretching energies. Using equations 2.2 through 2.4, the stored strain energy of the spring can be found with reasonable accuracy.

$$U_b = \frac{1}{2}\alpha R[D_{11}\kappa_x^2 + 2D_{12}\kappa_x(\kappa_y - \frac{1}{R}) + D_{22}(\kappa_y - \frac{1}{R})^2] \tag{2.2}$$

$$U_s = \frac{A_{11}}{2}[\frac{\alpha R}{2}\frac{\kappa_x^2}{\kappa_y^2} + \frac{\sin{(\alpha R\kappa_y)}}{2}\frac{\kappa_x^2}{\kappa_y^3} - \frac{4\sin{(\alpha R\frac{\kappa_y}{2})}^2}{\alpha R}\frac{\kappa_x^2}{\kappa_y^4}] \tag{2.3}$$

$$U = U_b + U_s \tag{2.4}$$

The strain energy path of a tape spring may look like the one shown in Figure 2.3. The internal strain energy is subject to relaxation as the spring is left in its stored configuration, which is also reflected in the figure. The behavior of the spring can therefore be expected to change when left stowed for too long.

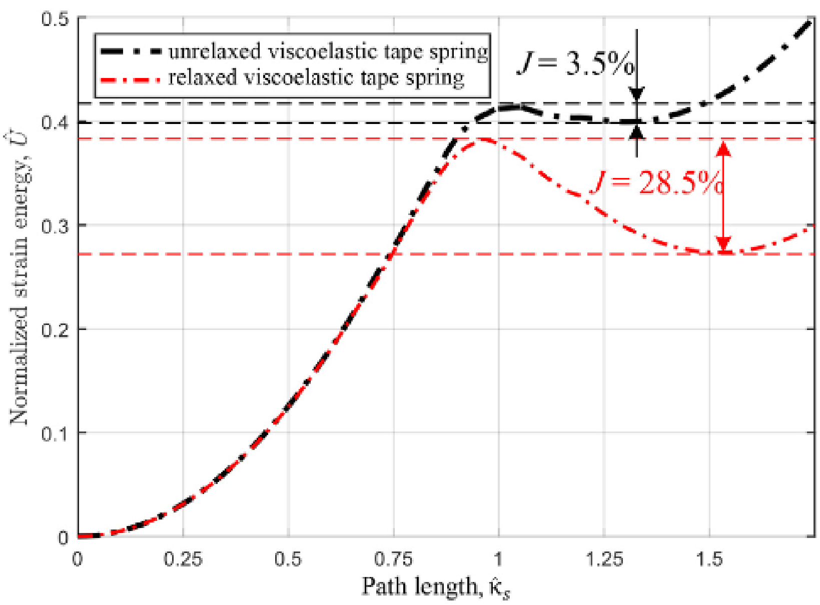

Figure 2.3: Typical strain energy in a bi-stable tape spring, before and after energy relaxation [23]

Based on the energy profile, a spring deployment method can be selected. The spring can be left to deploy freely if the stored strain energy is low. Free deployment is simple, but high amounts of stored energy lead to overshoot motions and shock loads. If energy levels are high, then a motor can be used to guide the deployment of the tape spring, as was the case for the aforementioned InflateSail satellite. Motor-controlled deployment gets rid of unwanted shocks and overshoot motions, but adds mass and complexity to the system. If desired however, the motor can also be used to retract the spring.

2.2. Neutrally Stable Tape Spring

In 2004, Murphey and Pellegrino [17] first theorized the creation of a neutrally stable tape spring, which is a type of tape spring that theoretically stores an equal amount of strain energy at any point along its deployment path. This means that the spring has no tendency to change position on its own. As a result, the spring can be actuated using very small forces, such as those provided by shape memory alloy (SMA) wires and piezoelectric films, as no internal change of energy has to take place. This leads to an actuator that can perform large shape changes with little energy input. In the project conducted by Murphey and Pellegrino, these springs were created by manufacturing two plies, in different pre-stressed configurations, which were then bonded together. Although the springs were shown to be close to neutrally stable in the short term, the property quickly degraded with time due to stress relaxation. The manufacturing process also proved to be cumbersome and difficult to control for quality.

Schultz et al [22] picked up on the idea in the following years and attempted to improve the concept by applying a different methodology. It was theorized that the deploying tendency of a tape spring could be negated by engineering the spring such that the internal spring-out moments are close to zero.

Within classical laminate theory, the internal moments due to bending are represented by the D section of the ABD matrix in Equation 2.1, or:

$$\begin{bmatrix} M_x \\ M_y \\ M_{xy} \end{bmatrix} = \begin{bmatrix} D_{11} & D_{12} & D_{16} \\ D_{12} & D_{22} & D_{26} \\ D_{16} & D_{26} & D_{66} \end{bmatrix} \begin{bmatrix} \Delta\kappa_x^{\circ} \\ \Delta\kappa_y^{\circ} \\ \Delta\kappa_{xy}^{\circ} \end{bmatrix} \tag{2.5}$$

By using plain-weave fabric plies, the simplification of $D_{16} = D_{26} = 0$ can be made. Using such plies in a balanced and symmetric layup leads to a laminate that has equal bending response in both x and y directions, or $D_{11} = D_{22}$. Assuming that the curvatures of the spring are equal over the two axes in the post-buckled state of equal-sense bending, or:$\Delta k_y = -\Delta k_x$, Equation 2.5 then simplifies to:

$$M_x = (D_{11} - D_{12})\Delta k_x^{\circ} \tag{2.6}$$

$$M_y = (D_{12} - D_{11})\Delta k_x^{\circ} \tag{2.7}$$

Equations 2.6 and 2.7 show that as D_{11} and D_{12} approach each other, the internal spring-out moments tend to zero. Schultz et al theorized that this creates a tape spring that is, in practical terms, neutrally stable, as a small amount of internal strain energy is typically dampened by internal friction. To better illustrate this, the energy balance in a tape spring can be simplified in Equation 2.8. When the tape spring is in its stowed (rolled up) position, the internal strain energy from the flattened curved shape drives a deploying motion, which is counteracted by internal friction in the tape spring. In a bi-stable spring, this strain energy is larger than the internal friction, and the spring will naturally deploy. For a neutrally stable tape spring, the strain energy is smaller than the internal friction and reduces further as the laminate is made more neutrally stable. An external force is then required to tip this balance to a positive outcome and start a deploying motion.

$$E_{total} = E_{strain} - E_{friction} \tag{2.8}$$

Schultz et al uses the definition of the laminate bending Poisson's ratio to illustrate the difference in D_{11} and D_{12}, as shown in equation 2.9. As this ratio approaches one, the tape spring is expected to become more stable, as the internal strain energy is further reduced and the gap between strain and friction energy increases.

$$\bar{\nu}_{xy} = D_{12}/D_{11} \tag{2.9}$$

As will also be shown in chapter 2.2.1, a large contributing factor to the D_{11} and D_{12} variables is the shear stiffness of the matrix. Schultz et al therefore theorize that a composite which utilizes a matrix with a low enough shear stiffness should lead to a neutrally stable tape spring when the internal moments are sufficiently reduced. Three different matrix materials were tested in the Schultz project. The theoretical results are summarized in Table 2.1. Use was made of an intermediate-modulus carbon fiber, namely 85 gsm plain-weave T300.

	Shear stiffness G [GPa]	**D$_{11}$**	**D$_{12}$**	**Bending Poisson's ratio ν_{xy}**
CTD-5XQ	0.198	0.162	0.156	0.963
CTD-10XQ	0.432	0.169	0.157	0.929
CTD-BG1.3	1.14	0.187	0.160	0.856

Table 2.1: Theoretical values for three resins tested by Schultz et al [22]

Of the three manufactured tape springs, CTD-5XQ was the only resin that provided a reliable neutrally-stable tape spring. CTD-10XQ showed stability at some points along the deployment path, and CTD-BG1.3 was not neutrally stable. All springs were at the very least bi-stable.

Schultz et al theorized that these neutrally stable tape springs could be used for various applications. Mentioned in the paper are a self-regulating radiator that changes surface area depending on temperature conditions, a roll-up deployable solar array that deploys a large-surface solar panel from a small rolled-up volume, and the application tested as a demonstrator for the paper: a deployable arm. The latter application is especially interesting for antenna deployment which is the topic of this research project. The deployable arm requires only a small electrical input, which heats an SMA wire and actuates the arm from the stowed to the deployed configuration. Such a mechanism provides the benefits of a motor-controlled bi-stable spring deployment, namely the prevention of shocks and overshoot motions. At the same time, it is less complex, consisting of no moving parts and requiring no lubrication. As indicated by the other concept designs in the paper, the idea of an SMA-actuated neutrally stable tape spring offers future applications for the deployment of other satellite appendages, which is a secondary objective of this research project. Based on these considerations, the decision was taken to select the neutrally stable tape spring concept for further study in this thesis.

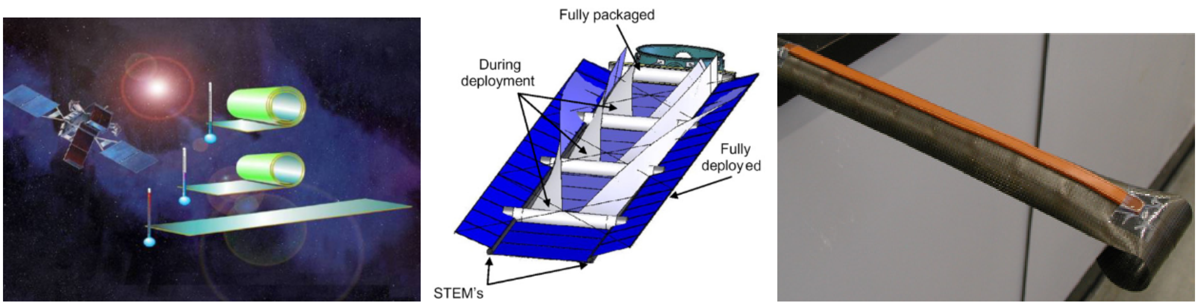

(a) Self-regulating radiator (concept) **(b)** Roll-up solar array (concept) **(c)** SMA-actuated deployable arm (built)

Figure 2.4: Devices using neutrally stable tape springs [22]

2.2.1. Sensitivity Study

In order to gain insight into the effect of the mechanical properties of the fiber and matrix properties on the expected neutral stability of the tape spring, a sensitivity study was conducted using a Python script. The parameters considered in the study are shown in Table 2.2, including their baseline values from the Schultz et al paper. The fiber volume fraction is unknown and was estimated by finding the value that best agrees with the results as they were published in the paper and shown in Table 2.1.

Property	Short	Magnitude	Unit
Fiber longitudinal stiffness	E_{1f}	233	[MPa]
Fiber transverse stiffness	E_{2f}	23.1	[MPa]
Fiber shear stiffness	G_{12f}	8.96	[MPa]
Fiber Poisson's ratio	ν_{12f}	0.2	[-]
Fiber volume fraction	V_f	0.392	[-]
Matrix Poisson's ratio	ν_m	0.36	[-]
Matrix shear stiffness	G_{12m}	0.198	[MPa]

Table 2.2: Sensitivity study baseline variables

The sensitivity study was performed by varying the material properties in Table 2.2 by a positive or negative change of 20%. The effects on D_{11} and D_{12} and resulting changes in ν_{xy} are then recorded. The results are shown in Figure 2.5.

From the results of the study, it is observed that a decrease in matrix shear stiffness G_{12m} provides the largest increase $(+0.47\%)$ to the laminate bending Poisson's ratio, leading to the largest benefit to neutral stability. Interestingly, increase in fiber longitudinal stiffness E_{1f} $(+0.35\%)$ and increase in fiber volume fraction V_f $(+0.10\%)$ also result in large increases in ν_{xy}. However, only the decrease in shear stiffness has been confirmed to be beneficial in the research of Schultz et al.

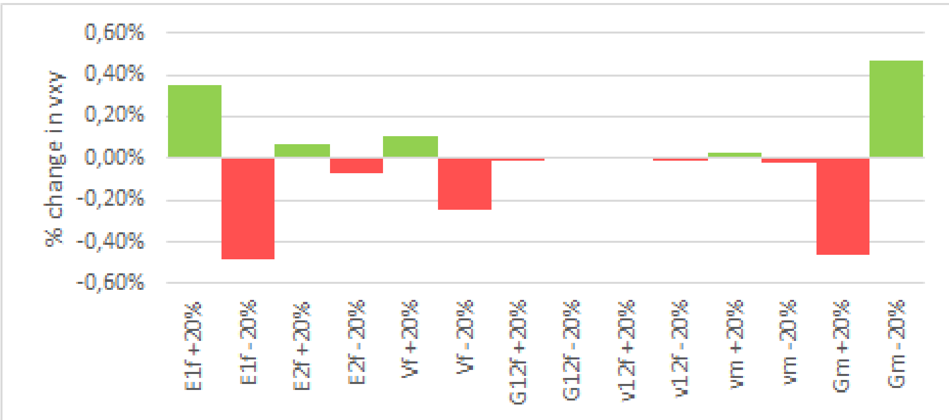

Figure 2.5: Effects of increases and decreases of fiber and matrix mechanical properties on neutral stability criterion ν_{xy}

2.3. Shape memory alloys

In summary, when a tape spring is sufficiently neutrally stable, internal friction keeps the spring from deploying itself. To deploy a tape spring from its stored position, this internal friction of a tape spring must be overcome by an external force to push the spring along its deployment path. In this project, such force is provided by a wire made of SMA. SMAs are a special class of metallic alloys that have the ability to contract and change shape under the influence of temperature.

SMAs have two main phases. The first is the high-temperature *austenite* phase, and the second is the low-temperature *martensite* phase. When austenite is cooled, it will begin to transform in to martensite. This transformation starts at a martensitic start temperature M_s and finishes at a lower martensitic finish temperature M_f. At this point the material is in a state known as *twinned martensite*. This transformation process is called the *forward transition*. Martensite can contain many different orientations of crystals within its lattice. These orientations are known as *variants*. The initially formed twinned martensite contains a large distribution of variants. Applying sufficient stress reorients the crystal structure, until a specific variant becomes dominant, known as a *detwinned martensite* state. A visible change in shape has also taken place. The minimum stress required to detwin martensite and change the shape of the material is known as the *detwinning start stress* σ_s. The martensite is fully detwinned when a *detwinning finish stress* σ_f is reached. The detwinned martensite, in its new shape, can now be heated to initiate a *reverse transformation* from martensite back to austenite. This transformation begins at an *austenitic start temperature* A_s and ends at an *austenitic finish temperature* A_f. When the austenite phase is reached, the SMA has regained its twinned martensite shape, before stress was applied. Subsequent cooling of the SMA brings it back to a state of twinned martensite, where it can be deformed again. The cycle of cooling, shaping, heating and restoring can be repeated, and thus used as an actuating force. Using temperature to cycle through the martensite and austenite phases is known as the *shape memory effect*, and it is this effect that will deliver the actuation force in this project.

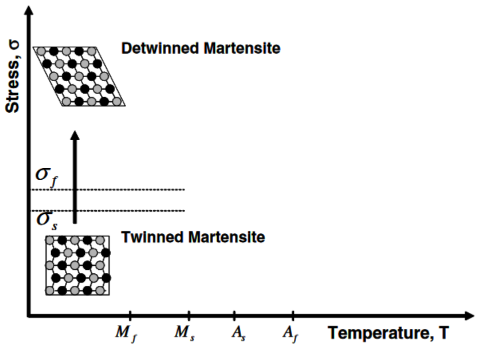

(a) Detwinning of martensite

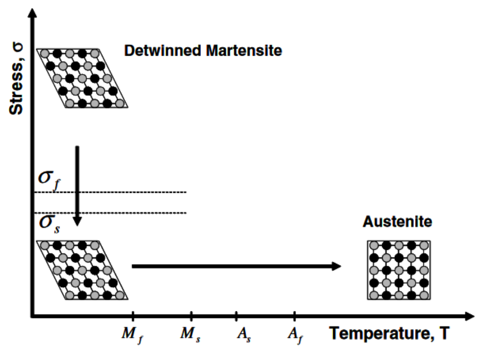

(b) Reverse transformation

Figure 2.6: Basic SMA transformations under stress and temperature [11]

The temperatures at which a phase transformation takes place between austenite and martensite varies with the applied stress. This is visualized in Figure 2.7a. When a stress is applied to the material, the temperatures at which the phase transformations take place are increased, visible as linear relationships in the figure. When the stresses involved are sufficiently high, it becomes possible to perform a phase transformation at a constant temperature, as seen in Figure 2.7b. For a temperature above M_s, fully detwinned martensite can be created from austenite by increasing the applied stress. This is known as *Stress-Induced Martensite (SIM)*. For a temperature above A_f, it is also possible to return the material to austenite by decreasing the applied stress. Similar to a thermally induced transformation, a shape recovery takes place upon returning to the austenite phase. Such a transformation cycle where strain is isothermally recovered under mechanical loading and unloading is known as the *pseudo-elastic* or *super-elastic effect*. The effect can be used to absorb energy without residual strain.

A pseudo-elastic cycle is shown in Figure 2.8a. Starting from A_f, the stress is increased until martensite starts to form at M_s. During the formation of martensite until M_f, the increase of strain per unit stress

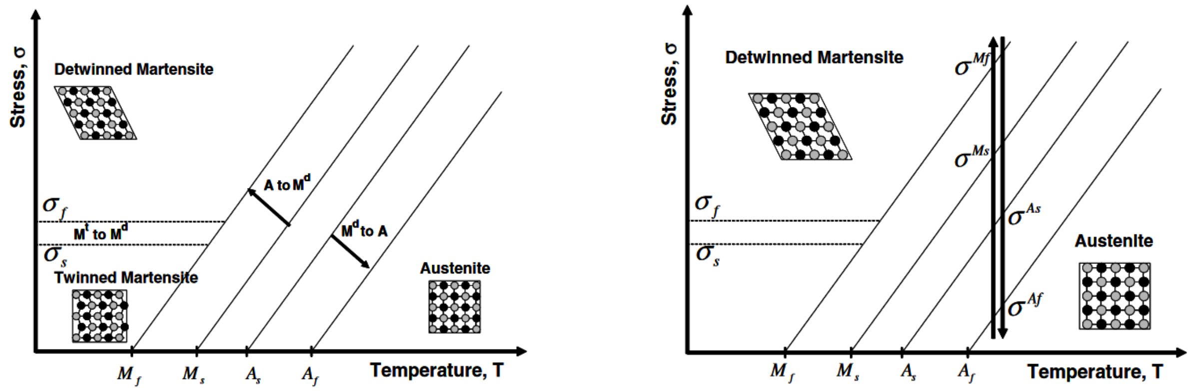

(a) Variation of transition temperatures with stress **(b)** Reverse transformation

Figure 2.7: Influence of stress on transition temperatures [11]

is much larger, but the stress remains below the plastic yield stress for the material. Subsequent unloading of the material leads to a phase change to austenite, as well as visible shape recovery, shown as a decrease in strain. Figure 2.8b shows a phase diagram including all three variables discussed so far.

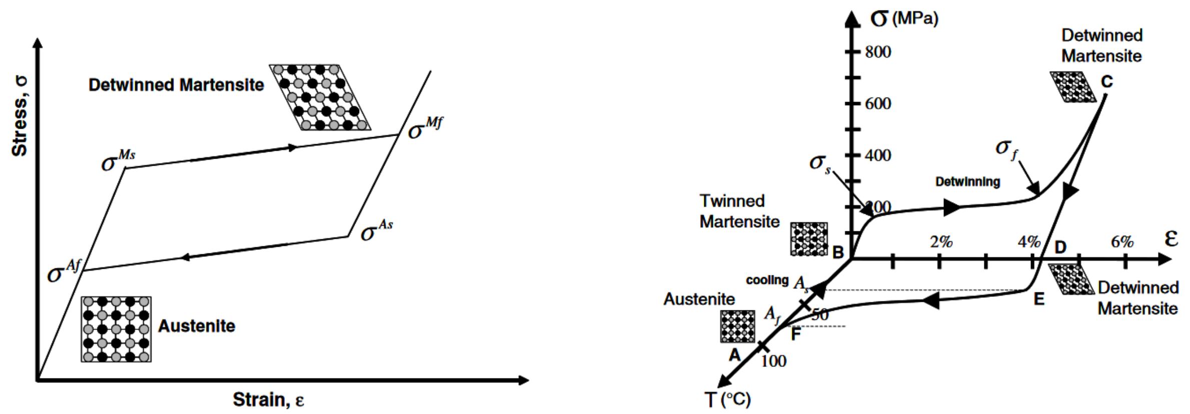

(a) Variation of strain during pseudo-elastic loading cycle **(b)** Phase diagram including strain, temperature and stress

Figure 2.8: Strain in transformation cycles [11]

As the name Shape Memory Alloy suggests, the material consists of multiple constituent metals. It is important to note that the exact composition of the alloy has a large effect on the transition temperatures. It is thus possible to tailor an SMA to the conditions it is intended to function in, not only by choosing the metals included in the alloy, but also by varying the fraction of each metal. Table 2.3 shows the large impact that varying compositions can have and gives an idea of operating temperatures. In the context of this project, a small supply of power will be required in order to heat up a wire beyond the temperature above which a transition to austenite is achieved.

NiTi Based SMAs	M$_f$	M$_s$	A$_s$	A$_f$
$Ti_{50}Ni_{50}$	15	55	80	89
$Ti_{49.5}Ni_{50.5}$	-78	-19	9	53
$Ti_{49}Ni_{41}Cu_{10}$	8	30	35	50
$Ti_{50}Ni_{40}Cu_{10}$	21	41	53	67
$Ti_{44}Ni_{47}Nb_9$	-175	-90	-85	-35
$Ti_{42.2}Ni_{49.8}Hf_8$	50	69	111	142
$Ti_{40.7}Ni_{49.8}Hf_{9.5}$	61	90	118	159
$Ti_{40.2}Ni_{49.8}Hf_{10}$	103	128	182	198
$Ti_{35.2}Ni_{49.8}Hf_{15}$	95	136	140	210
$Ti_{48}Ni_{47}Zr_5$	20	65	75	138
$Ti_{43}Ni_{47}Zr_{10}$	45	100	113	165
$Ti_{38}Ni_{47}Zr_{15}$	100	175	175	230
$Ti_{50}Ni_{45}Pt_5$	10	29	36	49
$Ti_{50}Ni_{40}Pt_{10}$	-8	18	-27	36

Table 2.3: Transition temperatures for several SMA alloy compositions [°C] [11] [26]

Table 2.4 furthermore shows typical mechanical properties for three types of SMA alloys.

Property	Ni-Ti	Cu-Zn-Al	Cu-Al-Ni
Melting point [°C]	1250	1020	1050
Density [kg/m^3]	6.45	7.9	7.15
Thermal expansion coefficient [$10^-6/K$]	6.6-10	17	17
E-modulus [GPa]	95	70-100	80-100
UTS, martensite [MPa]	800-1000	800-900	1000
Elongation to fracture, martensite [%]	30-50	15	8-10
Fatigue strength [MPa]	350	270	
Transformation temperature range [$°C$]	-100 to +110	-200 to +110	-150 to +200
Maximum one-way memory strain [%]	7	4	6
Normal two-way memory strain [%]	3.2	0.8	1
Normal working stress [MPa]	100-130	40	70
Normal number of thermal cycles	+100,000	+10,000	+5,000
Maximum overheating temperature [$°C$]	400	150	300
Damping capacity [%]	20	85	20
Corrosion resistance	Excellent	Fair	Good

Table 2.4: Properties of typical Ni-Ti, Cu-NI-Al, Cu-Zn-Al alloys [30]

The SMA's memory in the martensite phase is created by *training* the SMA, performed by repeatedly applying a thermo-mechanical cycle to the material. This causes small but permanent defects leading to a permanent internal stress state, causing a small part of the induced strain of the cycle to be unrecoverable. The additional permanent strain that is introduced decreases for each additional cycle until the permanent strain remains practically constant, at which point the material has assumed a new memorized shape. This is shown in Figure 2.9 at a level of approximately 2,7%. It is therefore important to consider the possible need of training for a mechanism made of SMA, in order to ensure accurate and reproducible operational cycles [30]. Training an SMA is a sensitive process. The final result of the training process is also sensitive to the training method, which must be carefully chosen [11]. It is susceptible to manufacturing defects such as small errors in alloy composition [7]. When properly controlled, a two-way SME response is also achievable and generally becomes stable after training for 10-30 cycles [25] [27]. This enables an SMA to have a memorized shape in both the martensite and austenite phases, allowing a single wire to provide both deploying and stowing motions if it can be kept above its austenite finish temperature or martensite starting temperature for the complete duration for which the actuator has to remain in the deployed or stowed configuration. However, this is likely to be unfeasible for the satellite antenna deployment case considered in this thesis.

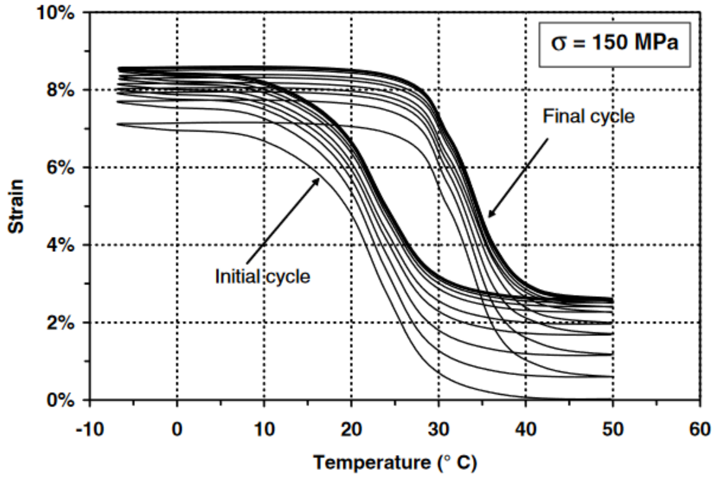

Figure 2.9: Acculumated permanent strain in transformation cycles [11]

3

Thermal Modeling

3.1. Modeling Background

The operating temperatures of the alloy must be known to select an SMA material. The goal of this chapter is to establish the thermal operating environment of the tape spring mechanism when attached to an orbiting satellite. The temperatures are important for the following reasons:

- The operating temperature affects the stiffness of the tape spring matrix material, which in turn affects the neutral stability characteristic of the tape spring as discussed in Chapter 2.2.1. An example variation of epoxy stiffness with temperature is illustrated in Figure 3.1;
- Shape memory alloys activate at specific temperatures as discussed in Chapter 2.3. These temperatures and as such the type of material must be chosen such that no spontaneous activation can take place during regular operating conditions.

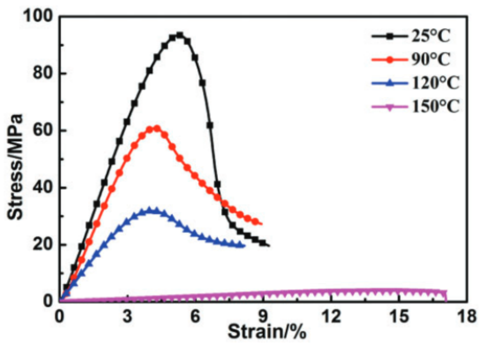

Figure 3.1: Changes in epoxy resin stiffness with temperature [12]

Delfi-Twin will be a rectangular triple-unit "PocketQube" that measures 50x50x178 mm, roughly the size of a half-liter milk carton, and the same size as its predecessor Delfi-PQ. The body is covered in black paint and has two 26 square centimeter solar cells on each of its long sides, for a total of eight. Thermal sensor data of Delfi-PQ was obtained during the satellite's mission and is available at [28]. Due to similarities between the two satellites, these data provide a unique opportunity to verify that the model that is to be created is accurate. The following methodology will be applied to accomplish this:

1. Create a simplified thermal model of the Delfi-PQ satellite;
2. Verify that the body temperatures match those seen in orbit for Delfi-PQ;
3. Add the tape spring geometry with its corresponding material properties to the satellite body;
4. Analyze the resulting in-orbit temperatures of the tape spring and establish operating temperatures.

The ESATAN model files are available in the 4TU research data repository [6].

3.2. Delfi-PQ data

Delfi-PQ temperature data is available online [28]. Four channels each measure the temperature on one side panel of the satellite bus. The temperature peaks are not uniform, as measurements are only transmitted depending on ground station availability and compressed to a smaller number of data points. The unknown orientation and position of the satellite at the time of measurement have an impact on the measured temperatures. A direct comparison between model and sensor data is therefore difficult, and only temperature peaks are used. Of the four measured panels, PanelYm is shown to be particularly hot. The difference between panels is possibly caused by the satellite's rotation axis not passing exactly through the geometric axis, caused by the center of mass not being in the geometric center and the density not being uniform. As it is not possible to know the exact orientation of the satellite at all times, the PanelYm temperatures will be taken as comparison data for the entire satellite. It is assumed that all panels on the satellite can reach this temperature, including the panel facing the tape spring. For the design of the tape spring assembly, a hottest worst-case scenario must be assumed. Underestimating the operating temperature can lead to higher than expected operating temperatures, exceeding the activation temperature of the SMA and causing unwanted actuation of the tape spring. The most relevant data to be observed are in January and July, which represent the perihelion and aphelion points in the Earth's orbit. These time frames are extracted from the online data and shown in Figures 3.2 and 3.3. The maximum temperature swing is approximately 70°C.

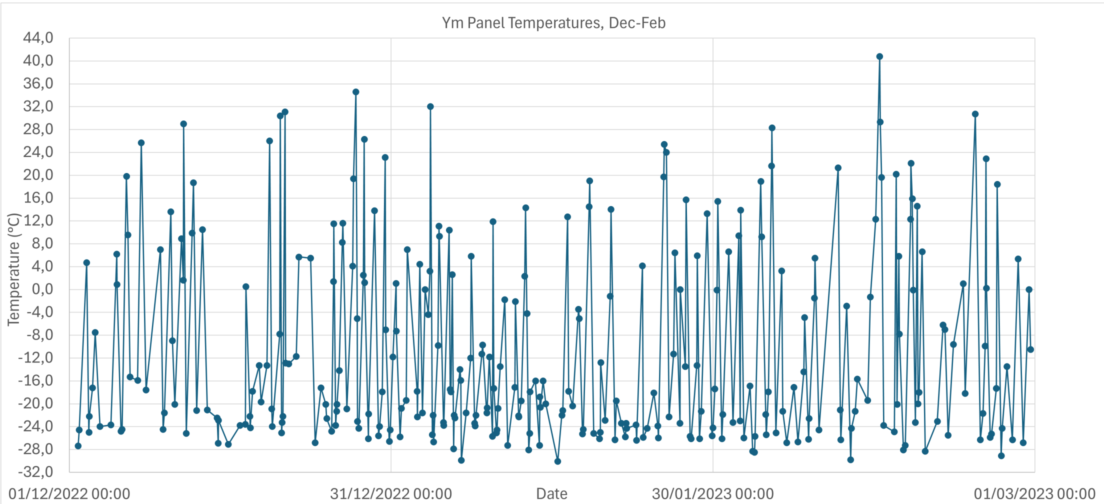

Figure 3.2: Body temperatures in January, PanelYm

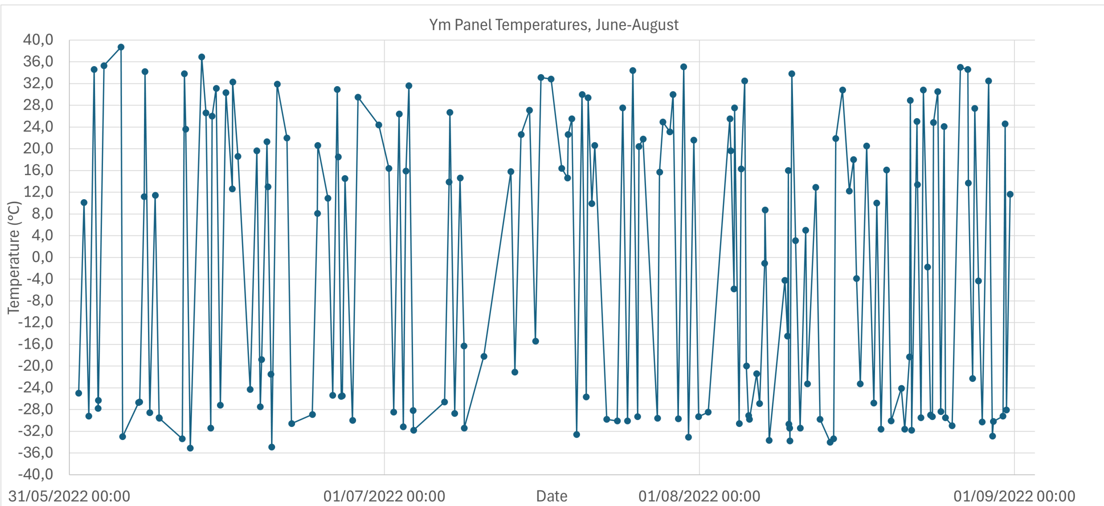

Figure 3.3: Body temperatures in July, PanelYm

	July [°C]	January [°C]
Maximum	38.7	40.8
Average high	36.2±1.43	33.84±3.74
Minimum	-35.1	-30.1
Average low	-34.3±0.58	-29.44±0.66

Table 3.1: Temperature data in Jun/Jul/Aug and Dec/Jan/Feb

Temperature data is summarized in 3.1, showing the temperature peaks, averages, and standard deviations based on the five most extreme temperatures. The data itself provide a somewhat distorted image. An important side note to be made is that in January, the satellite passes over ground stations mostly in or shortly after exiting eclipse. As a result, the real peak temperatures in January are not represented in the data. These peaks are expected to be several degrees higher than those in July due to Earth being at perigee relative to the Sun in January. The solar flux is therefore higher in January. For this reason, a temperature swing of a few degrees higher than that of July can be considered acceptable.

As the true maximum temperature data in January are unavailable, focus is placed on creating a model that is accurate for the data in July. A separate analysis can then be performed for the orbital case of January for the same tape spring model, which is then assumed to be accurate under otherwise equal conditions.

3.3. Delfi-PQ ESATAN Model

ESATAN-TMS is chosen as the thermal modeling software for this phase of the project. ESATAN has a simple built-in 3D model creation tool. These models can be used in radiative and thermal analysis cases. Radiative cases make use of monte carlo ray tracing (MCRT) techniques to study view factors and radiative exchange factors between components of a model. Thermal cases then process conductive, convective and radiative heat transfer with external radiative cases as possible inputs.

In the context of this project, a 3D model of the Delfi-PQ / Delfi-Twin satellites is created. It is exposed to a radiative case where the satellite is in orbit around the Earth and taking in direct solar flux from the Sun, albino flux from the Earth, infrared (IR) flux from the Earth, and any reflected energy from the satellite itself. Internal power from the satellite is also added as an input in the thermal case. The thermal case then processes the heat exchanges over time to find the temperatures of various components. For this project, points of interest are primarily the maximum and minimum temperatures of the satellite body and later attached tape spring.

The satellite bus is modeled as a simple rectangle measuring 50x50x178 mm. Data on material properties of the satellite, internal power, and orbit are obtained as follows.

Optical properties: the solar cells have an absorptivity of $\alpha = 0.91$ [1]. It is assumed that the emissivity for a gallium arsenide solar cell is $\epsilon = 0.82$ [20]. The exact properties of the black paint are unknown, but are assumed to be $\alpha = 0.96$ and $\epsilon = 0.82$ (within a realistic range of 0.75-0.88 given in [20]). Given that the solar cells cover approximately 70% of the surface area of the satellite, the assumed combined properties are averaged as $\alpha = 0.93$ and $\epsilon = 0.82$ for the surface of the satellite bus.

Thermal properties: the satellite frame is made of aluminum, with other materials comprising the interior. Aluminum has a specific heat capacity of 0.9 $\frac{J}{g \cdot °C}$ [14]. The thermal capacitance of the satellite is added to the model using a combination of wall thickness in the rectangle and a non-geometric node inside of the rectangle, along with the appropriate conductive and radiative links.

Internal power: the satellite is expected to generate an internal power between 0.2 W and 0.3 W. Preliminary simulations have shown that the resulting difference in the maximum temperature of the tape spring is in the order of less than 0.01 °C. As a result of this negligible impact, an average value of 0.25 W is used for the internal power generation.

Orbit and dynamics: the satellite is in a sun-synchronous orbit with an inclination of 97°. This orbit is circular, with an apogee/perigee of 550 km after launch. The Delfi-PQ satellite was in space between January 2022 and January 2024, passing through 350 km of altitude approximately one month prior to decay [19]. An altitude of 350 km will therefore be taken as the lowest altitude to model, and steps of 50 km will be modeled after addition of the tape spring. Lastly, based on experience with Delfi-PQ, the satellite is expected to experience a longitudinal rotation of five degrees per second, which is implemented.

The axes of the satellite model are shown in Figure 3.4.

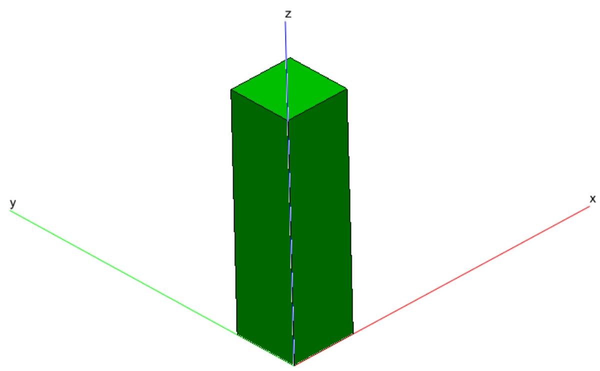

Figure 3.4: X (red), Y (green) and Z (blue, longitudinal) axes of the satellite

The orientation of the satellite makes a large difference in the amount of surface area facing the Sun. As a result, the absorbed solar flux can vary significantly, and with it the temperature profile of the satellite. Figures 3.5-3.10 show several scenarios.

- Case 1: Velocity oriented. The longitudinal axis faces in the velocity direction and slightly nadir; the satellite rotates a normal-to-orbit axis as it orbits. The side panels face the sun at the peak of the sun-lit phase. The top and bottom face the sun at eclipse entry and exit.
- Case 2: Normal to orbit. The longitudinal axis faces normal to the orbit and slightly nadir. The side panels face the sun during the entire orbit, but at a slightly varying angle.
- Case 3: Sun facing. The longitudinal axis of the satellite faces the sun at all times.

The time axes in these plots are cropped at 20.000 seconds. This is done to eliminate early transients in which the temperature range has not yet settled to a steady swing, as a result of the satellite starting out with an initial temperature that does not match its starting position in orbit. All orbits are clockwise, and the Sun vector is indicated by the yellow arrow emanating from the Earth's surface.

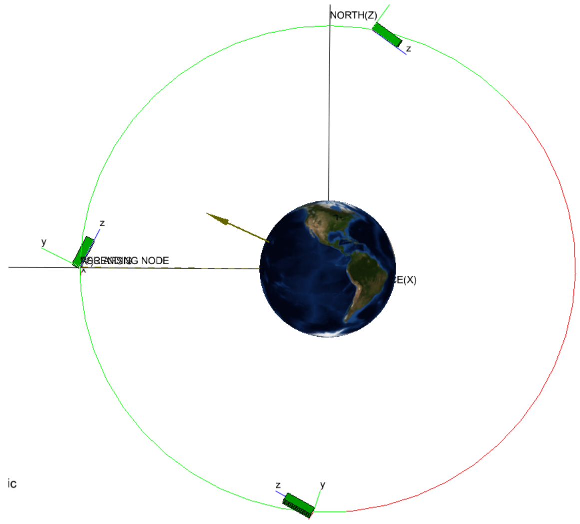

Figure 3.5: Satellite orientation of case 1

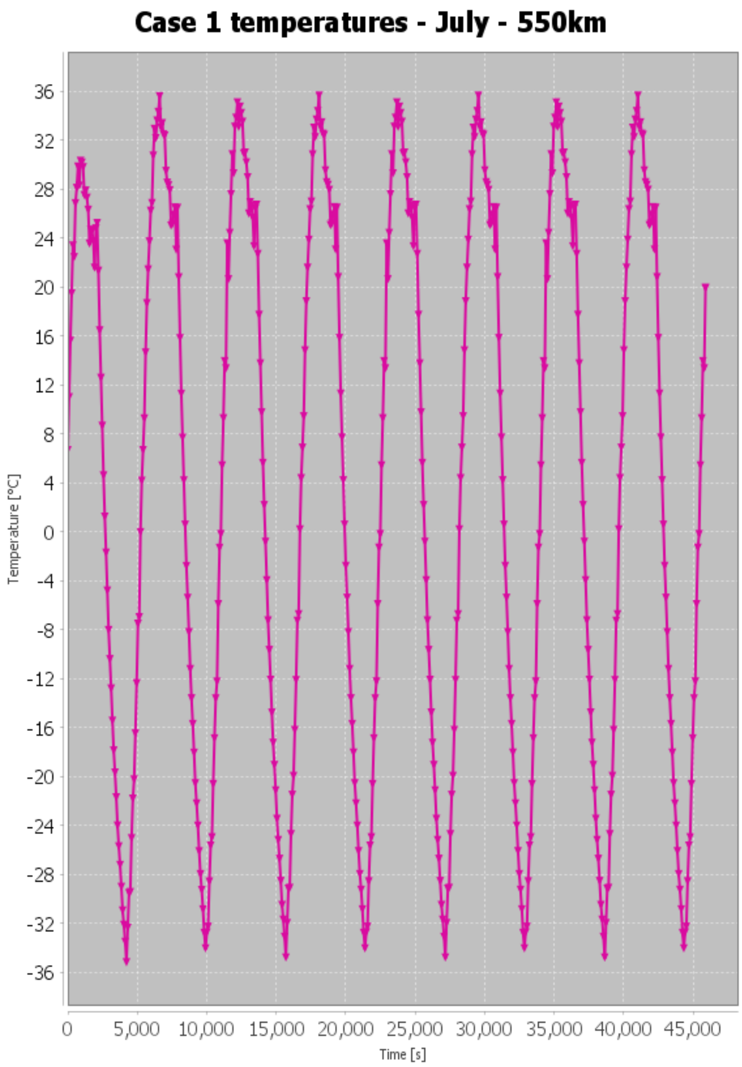

Figure 3.6: Temperature progression of case 1

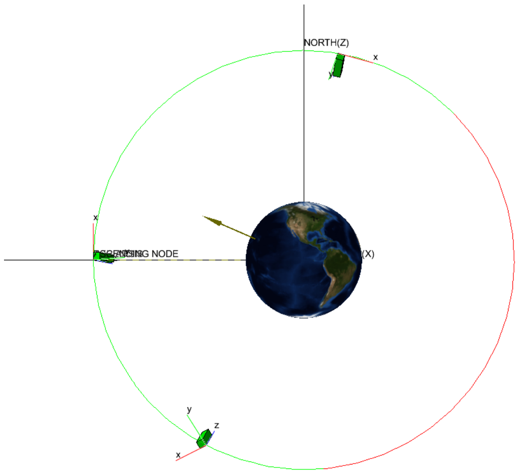

Figure 3.7: Satellite orientation of case 2

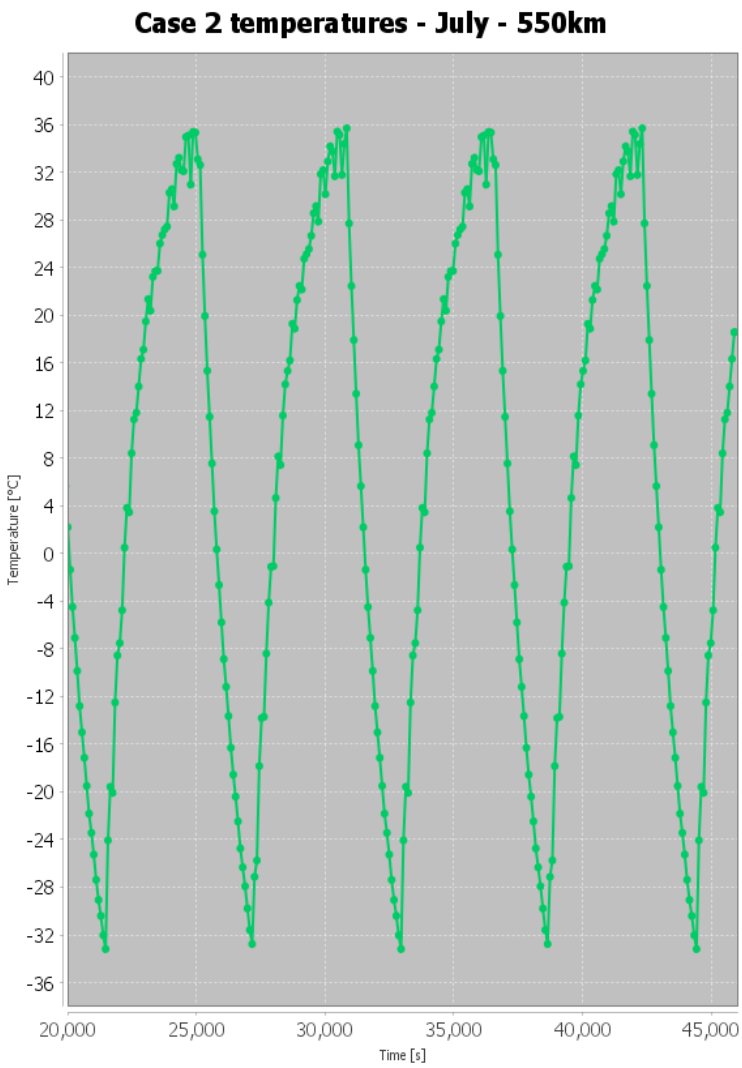

Figure 3.8: Temperature progression of case 2

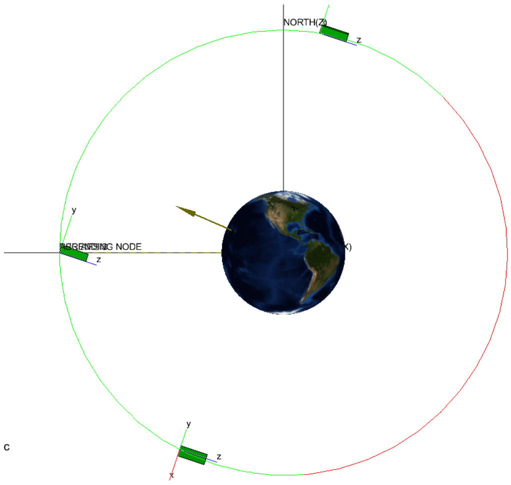

Figure 3.9: Satellite orientation of case 3

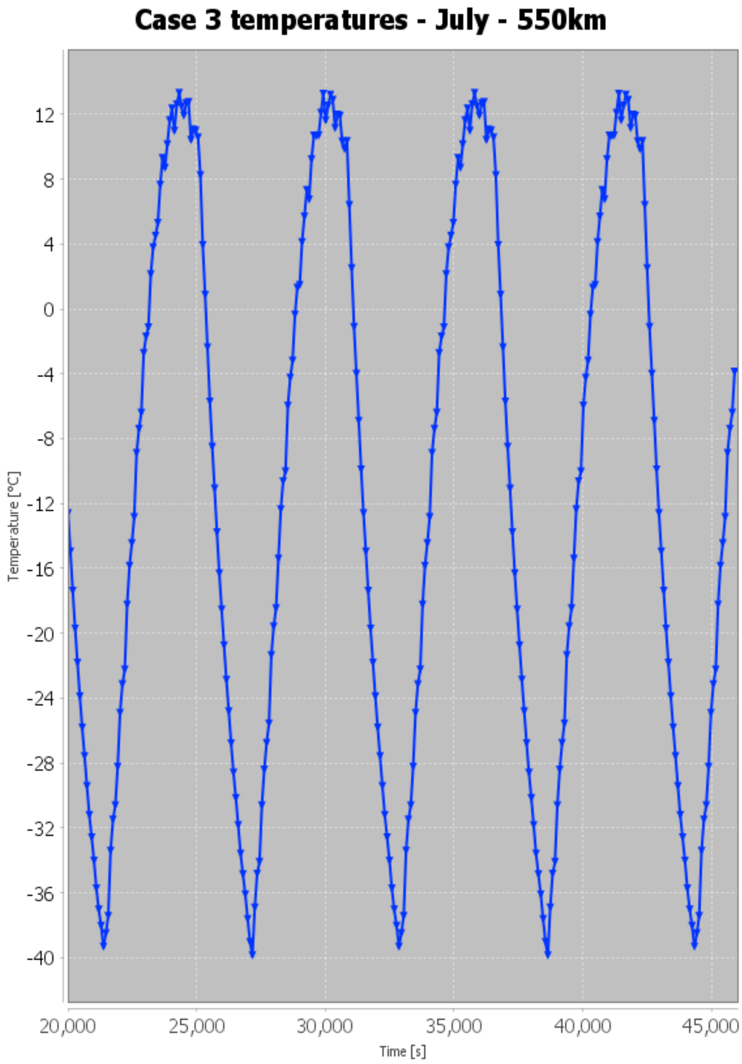

Figure 3.10: Temperature progression of case 3

The maximum and minimum temperatures for each case are shown in Table 3.3. Each case was also run in January. Case 3 is the coldest case for the satellite but it will be the hottest case for the tape spring. However, since the body temperature is lower compared to cases 1 and 2, the base of the tape spring can be expected to be colder due to conduction.

The total thermal capacitance used to model the satellite in these figures is 213$\frac{J}{K}$, which is equivalent to 236 grams of aluminum. This is considered acceptable, as the satellite itself has a total mass of 545 grams but is only partially made of aluminum, mainly in the frame. Other materials used on board include arsenic and gallium (solar cells), silicates, and other metals that have a lower specific heat capacity.

Table 3.2: Maximum and minimum temperatures of the three orbit cases [°C]

	July [max]	July [min]
Case 1	35.7	-35.2
Case 2	36.2	-33.2
Case 3	13.9	-40.1

Figure 3.11 shows the temperature progression of the three different cases, as well as the range of standard deviations from Table 3.1 for the high and low temperatures.

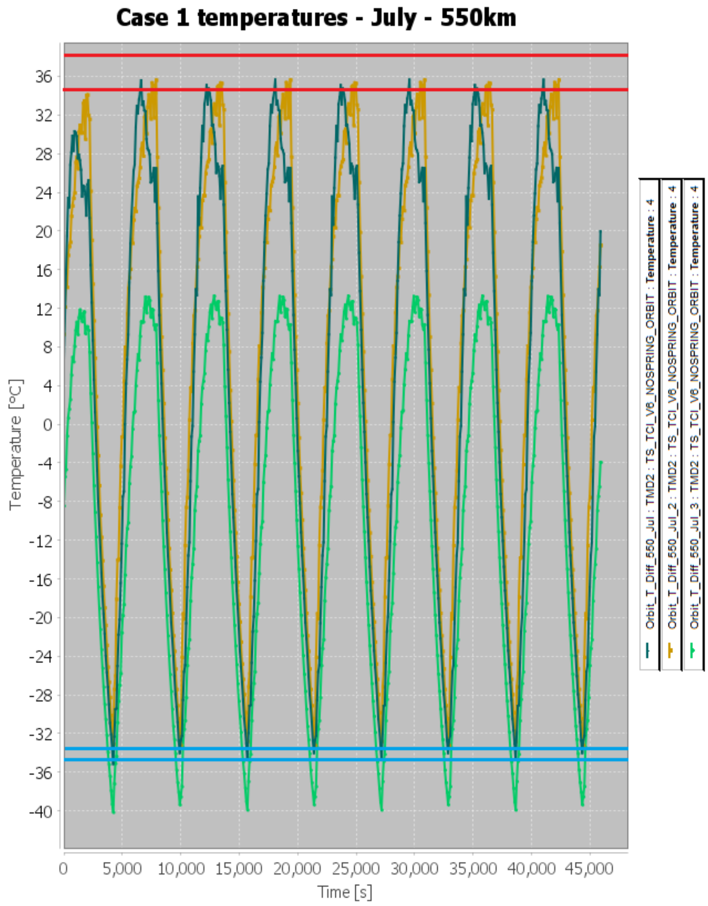

Figure 3.11: Temperature progression of cases 1-3 including standard deviation ranges from Delfi-PQ data

3.4. Model and data comparison and validation

It is not possible to draw a direct comparison between the temperature progression in the data and that of the models, as the real orientation of Delfi-PQ is unknown and data was received only intermittently. However, it is possible to compare the peak temperatures from the flight data with the peak temperatures of the three orbit cases. This is done by comparing Tables 3.1 and 3.2, resulting in Table 3.3.

Table 3.3: Differences in temperature extremes between ESATAN model and Delfi-PQ sensor data [°C]

	July [max]	**July [min]**
Case 1	0.4	-0.1
Case 2	0.9	1.9
Case 3	-21.4	-5

The temperature peaks are of interest because they show the total accumulated solar flux in a sun-lit phase. A lower peak temperature indicates that in parts of this phase, the satellite had its longitudinal axis pointed towards the sun, and less heat energy was accumulated in the side panels. This is particularly visible in the results for case 1, where the temperature starts to decrease while the satellite is still in sunlight, and briefly increases again before entering eclipse, as the side panels begin to orient towards the sun once more.

In general, cases 1 and 2 can be seen as covering a wide variety of possible orientations in orbit, where the satellite can further rotate around other axes besides the longitudinal one. The side and end panels are both exposed to sunlight for a large part of the orbit. From Table 3.3 and Figure 3.11, it is concluded that in these cases, the model agrees well with the data recorded by Delfi-PQ.

For case 3, peak temperatures on the side panels remain low. Most importantly, the average temperature is around -13 °C, whereas it is 0 °C for the Delfi-PQ data. Because the average temperature mostly shifts due to internal power generation and optical properties of the body, which are largely known, this case is unlikely to have occurred in real life. An orientation similar to case 1 or 2 is thus deemed likely, and the thermal capacitance is considered accurate for the model.

3.5. Tape spring addition

The satellite model is now expanded with a tape spring, modeled as a section of a cylindrical shell. The spring is attached to the edges of one of the side panels of the satellite bus. The dimensions and properties given to the tape spring are as follows:

Component	Property	Value
Spring dimensions	Radius [m]	0.015875
	Length [m]	0.36
	Angle [deg]	60
Spring material	Thickness [mm]	0.21
	Density [kg/m3]	1420
	Specific heat [J/kg.K]	1130
	Conductivity [W/m.K]	78.8
Spring optical	Emissivity ϵ	0.82
	Absorptivity α	0.92

Table 3.4: ESATAN tape spring properties

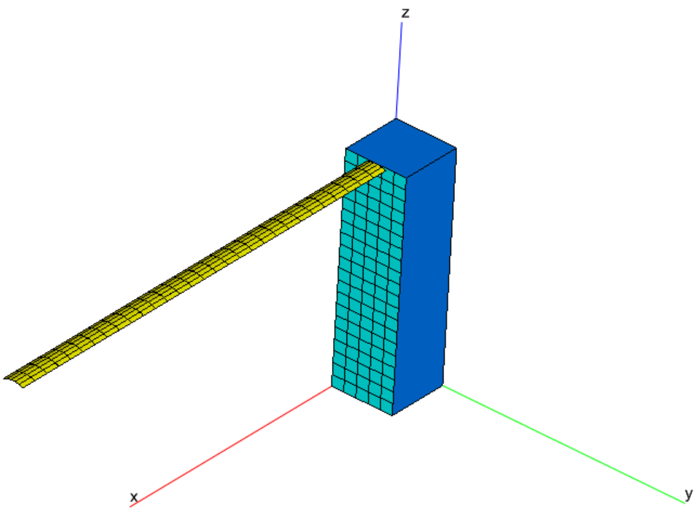

Figure 3.12: Tape spring added to the ESATAN satellite model

It was theorized that a more fine discretization of the body panel facing the tape spring was required to capture the interaction of reflecting solar rays between the tape spring and the body panel as precisely as possible. However, a brief study between panel discretizations of 3x14, 5x20 and 7x26 nodes only resulted in no more than a 0.01 degree difference in temperature at the free end of the tape spring. The panel discretization was therefore left at a mesh of 5x20 nodes.

A conductive link is added between the tape spring and the satellite bus to capture the conductive interaction between the tape spring and satellite. Specification of the link requires the conductivity k across the interface as well as the shape factor. Both are estimated using several assumptions.

The shape factor is defined in Equation 3.1:

$$S = \frac{A}{dx} \tag{3.1}$$

In this equation, A is the area and dx is the typical path length over which conduction takes place along the length of the spring. The area A is found using the thickness of the spring and the area of a cylindrical wall section. As the conductive link is specified from the closest node to the satellite bus and the satellite bus itself, dx is taken to be half the length of a node in x-direction along the spring. In the case of 30 nodes in lengthwise direction, this would equate to 6 mm for a 36 cm tape spring.

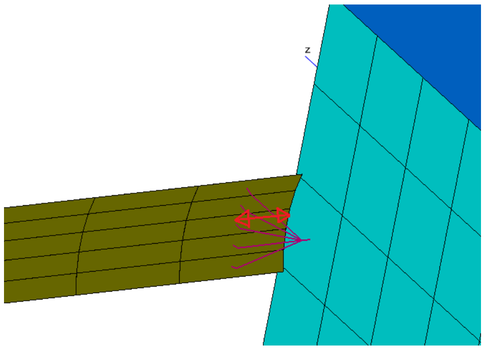

Figure 3.13: Path length specified for the shape factor calculation

The conductivity over the interface is dependent on the thermal conductivity of the two materials and the thermal boundary resistance, which is dependent on the boundary conditions. This boundary resistance is generally calculated using models such as the Acoustic Mismatch Model or Diffuse Mismatch Model. As the exact boundary conditions are unknown at this stage, a simpler approach is taken. The average of the thermal conductivities of the two materials (CFRP and aluminium) is taken, and a variation is tested to see whether the uncertainty in the conductivity is acceptable.

Using conductivities of 78.8 $\frac{W}{m \cdot K}$ [15] for CFRP and 210 $\frac{W}{m \cdot K}$ [14] for aluminum, an average of 144.4 $\frac{W}{m \cdot K}$ is found. Simulations are run for this value, as well as for 170.64 $\frac{W}{m \cdot K}$ and 118.16 $\frac{W}{m \cdot K}$, which split the difference 20% more in favor towards aluminum and CFRP respectively. The resulting temperatures for the node closest to the satellite bus are as follows:

Table 3.5: Temperatures of the tape spring node closest to the satellite bus for varying conductivity values, January, h = 550 km

Model	Conductivity [$\frac{W}{m \cdot K}$]	Spring nodes, w x l	Panel nodes, w x h	T max [°C]
Al favored	170.64	5 x 30	5 x 20	38.114
Average	144.4	5 x 30	5 x 20	38.419
CFRP favored	118.16	5 x 30	5 x 20	38.846

From this data it is concluded that the variation in temperature due to conductivity uncertainty is expected to be within a degree. As it is not possible to further define the conductive link at this stage of the project, this variation is considered acceptable. The average conductivity of 144.4 $\frac{W}{m \cdot K}$ is used further. For an accurate determination of this conductive behavior, testing is necessary. As the test conditions are dependent on the exact method of attachment to the satellite, this is left as future work.

Next, it is important to set a sufficiently fine orbital discretization in order to accurately capture the effect of the rotation of the satellite on the absorption of solar flux in different satellite surfaces. To this end, a convergence study is performed on the tape spring model with a tape spring mesh of 5x30 nodes using an orbital discretization of 90, 180, 360, 720, 1440 and 2880 points, or 4, 2, 1, 0.5, 0.25, 0.125 degrees of orbit angular resolution, respectively.

Between subsequent orbits, there is a variation in peak temperatures of the outermost tape spring node in a repetitive pattern. This pattern of four distinct peaks is shown in Figure 3.14.

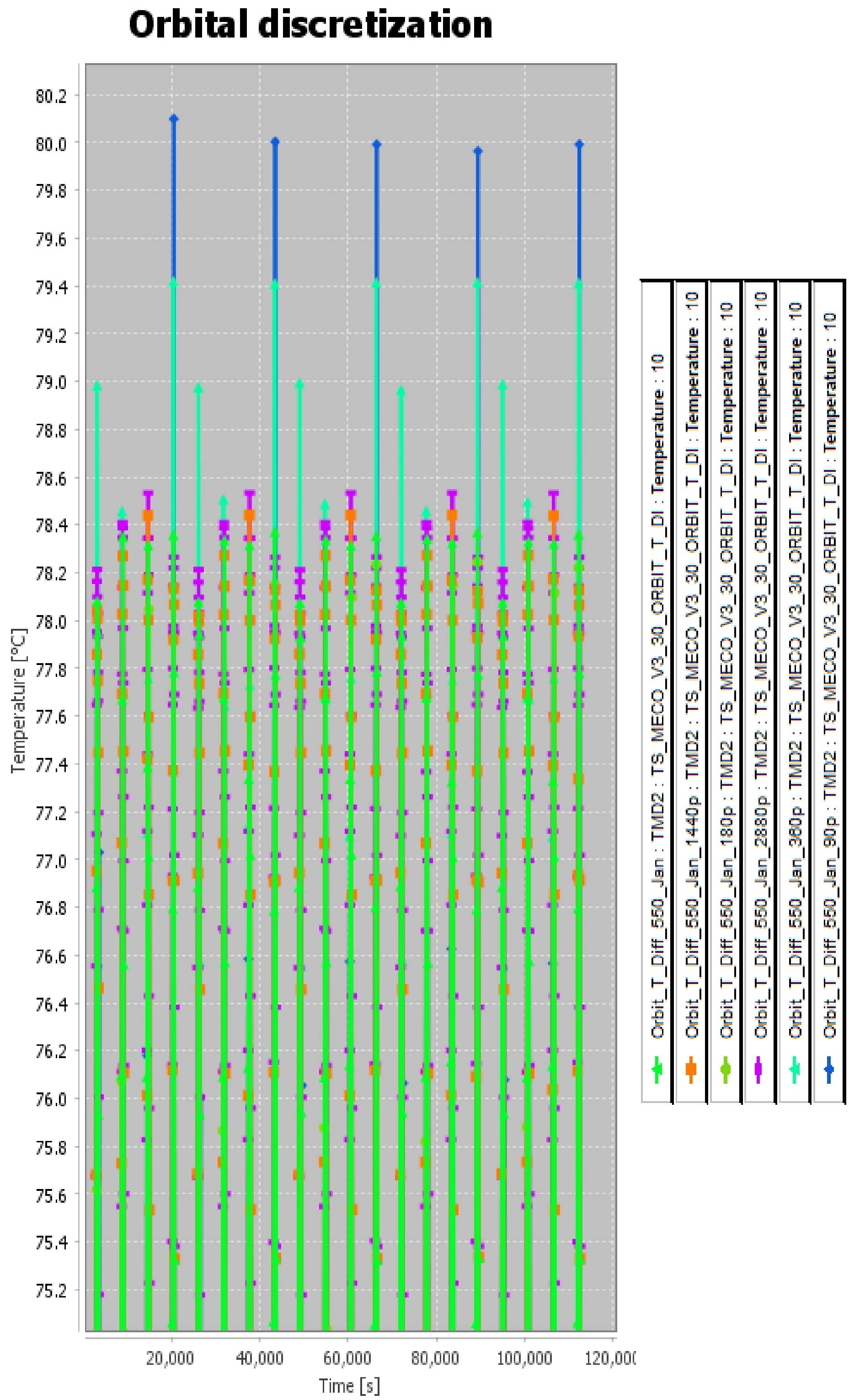

Figure 3.14: Repetivive pattern of peak temperatures

To visualize these differences, Table 3.6 and Figure 3.15 show the convergence for each of these peaks, as well as the computational time for each discretization. Given that the computational time for subsequently used larger tape spring meshes is up to six times higher (Table 3.7), the 720p resolution is taken as being sufficiently converged, as no major changes occur beyond this point and the spread between the different peak types becomes less than half a degree.

Nodes	Tmax, 1 [°C]	Tmax, 2 [°C]	Tmax, 3 [°C]	Tmax, 4 [°C]	Comp time [hh:mm:ss]
90p	72.21	76.57	79.99	76.08	00:01:31
180p	75.88	78.12	78.22	74.64	00:02:44
360p	78.50	77.76	79.41	78.99	00:05:14
720p	78.33	78.32	78.36	78.08	00:10:33
1440p	78.27	78.44	78.13	78.02	00:16:31
2880p	78.41	78.53	78.27	78.21	00:33:37

Table 3.6: Orbital discretization convergence data for four peak types

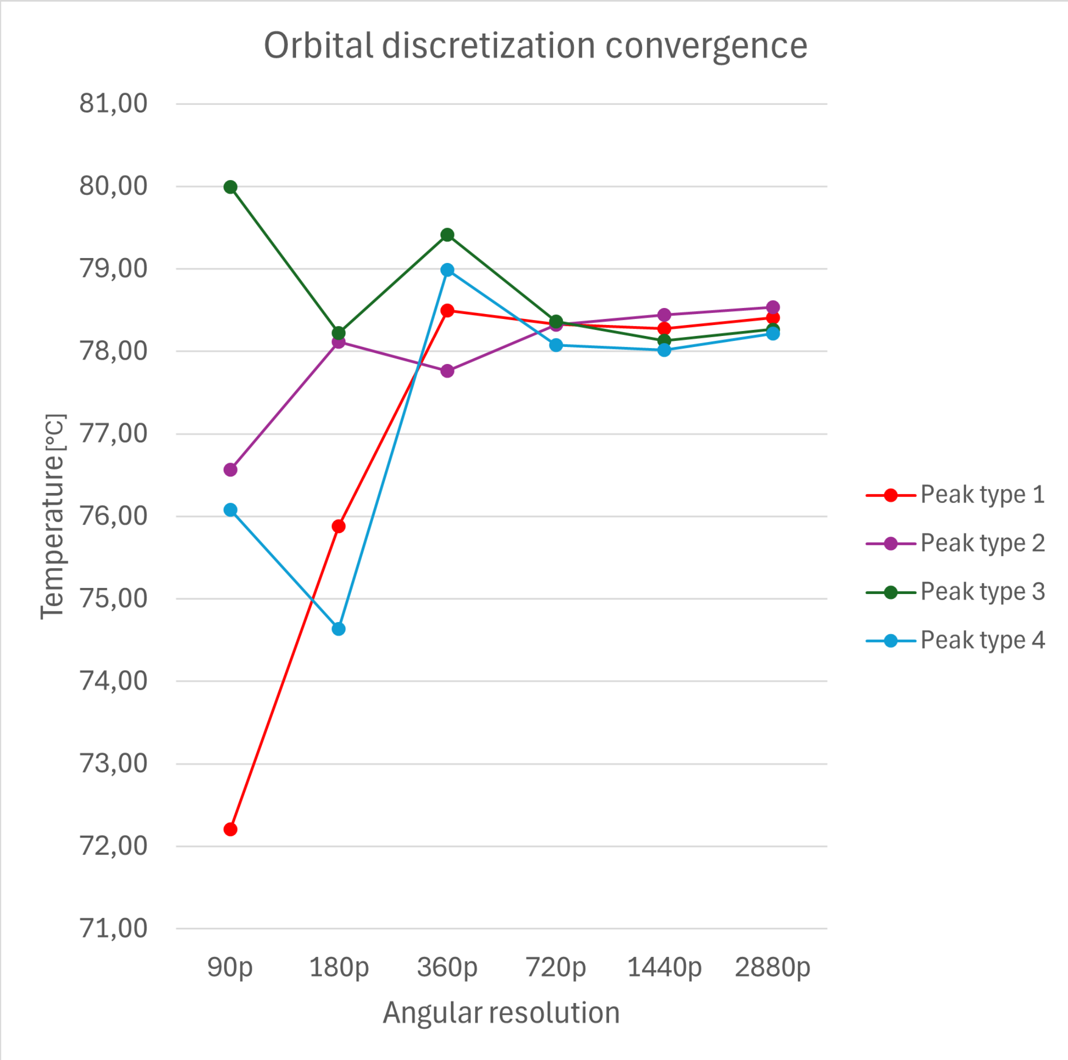

Figure 3.15: Orbit discretization convergence study plot

Finally, a mesh convergence study is performed on the tape spring itself to ensure sufficient model accuracy. To perform this study, additional nodes are added in the lengthwise direction (x-axis) of the tape spring. The conductive link is appropriately modified to account for the smaller tape spring nodes and resulting shorter path length. Models for 30, 60, 120 and 240 nodes in length were run. The results are shown in Table 3.7 and Figure 3.16. The model appears to converge to a temperature just over 40°C.

Table 3.7: Convergence study in to the temperature of the innermost node of the tape spring. January, h = 550km

Model	Run time [hh:mm:ss]	Spring nodes, w x l	Panel nodes, w x h	T max [°C]
30	00:10:40	5 x 30	5 x 20	39.35
60	00:15:40	5 x 60	5 x 20	39.682
120	00:26:50	5 x 120	5 x 20	39.861
240	01:02:40	5 x 240	5 x 20	39.976

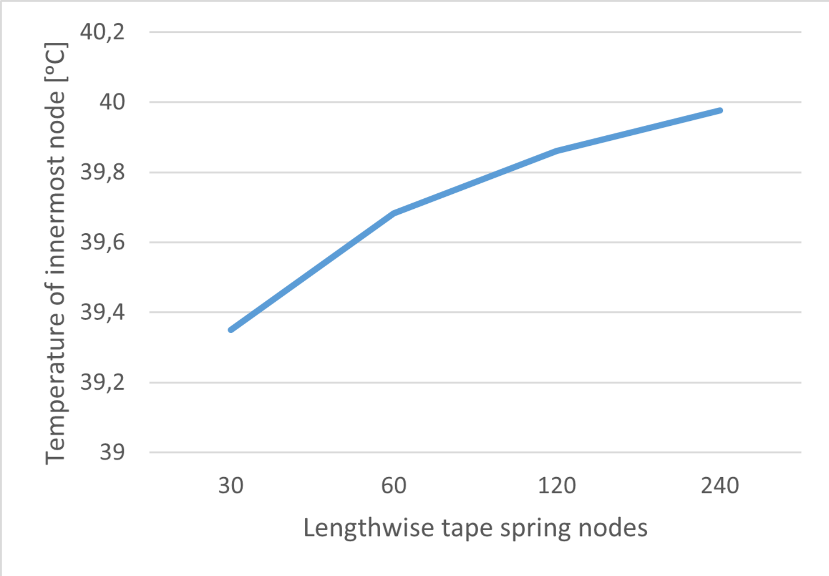

Figure 3.16: Convergence study results plot

3.6. Thermal Results

Models are now run at 50 km intervals between the expected launch altitude of 550 km and the estimated start of accelerated decay at 350 km. These are again performed for the months of July 2022 and January 2023, using an inclination of 97° as provided by the Delfi team. The model with 240 lengthwise nodes in the tape spring is used for the analyses.

Four data points are of interest from the thermal analyses: the hottest and coldest temperature cases of the tape spring, the largest thermal gradients across the length of the tape spring at one instance in time, and the largest thermal gradients in time at one node of the tape spring.
Plots are created using data extracted from the ESATAN models. Every fourth node along the length of the tape spring is used, as the ESATAN software struggles to plot a large number of nodes. The first and last nodes of the tape spring are always included in order to capture temperature extremes.

Along with the minimum and maximum temperatures, the maximum temperature gradients over time as well as those over the length can be extracted from the model data.

Figure 3.17 shows the minimum and maximum temperatures along the length of the tape spring. The respective coldest or hottest point on the tape spring is plotted, with the remaining temperatures across the length belonging to the same time stamp. The figure shows that the maximum temperature varies not only with altitude but also with time of year. As discussed before, this is expected because the Earth is closer to the Sun in January and the solar flux is at its highest. The minimum temperature does not change with the time of year. A slight increase is caused by either the increased IR flux from Earth from flying at a lower altitude and/or the higher peak temperature reached in sunlight.

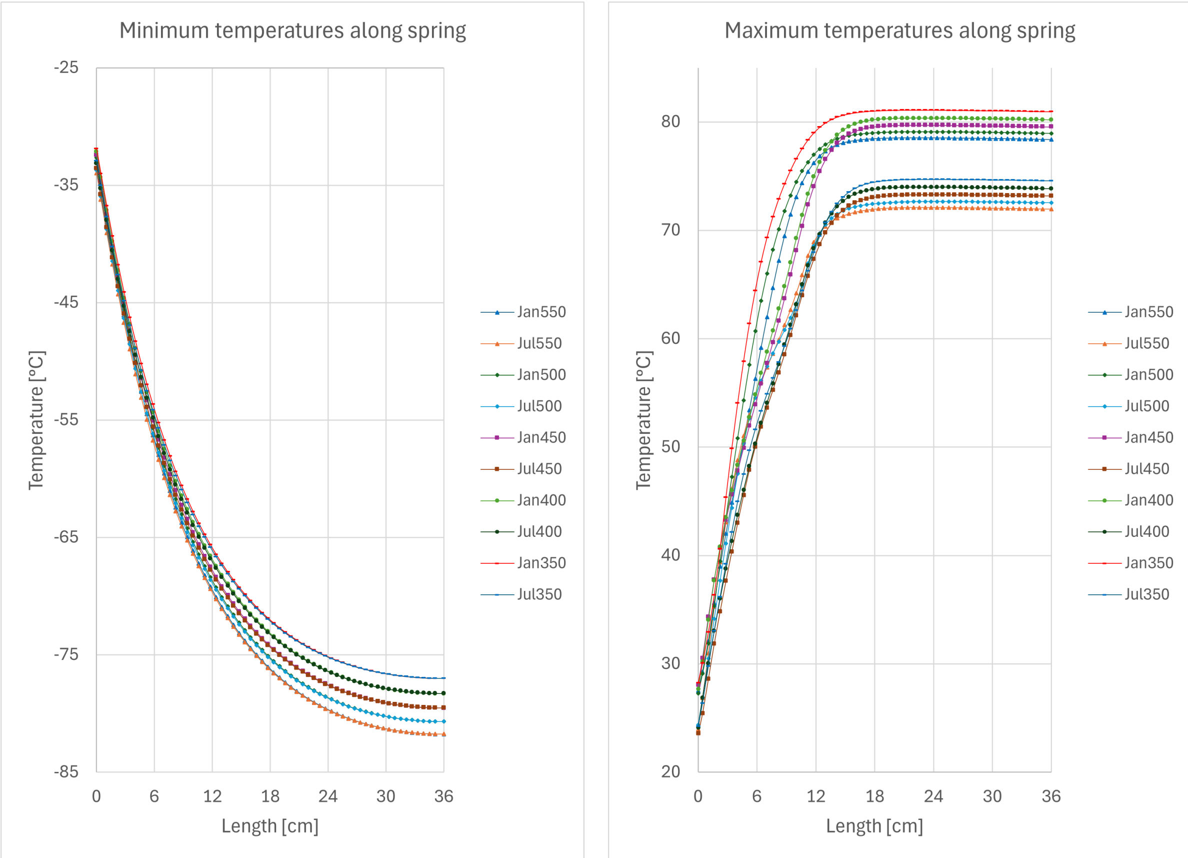

(a) Minima

(b) Maxima

Figure 3.17: Minimum and maximum temperatures along the length of the tape spring

	$\Delta_{T_{t,max}}$	$\Delta_{T_{t,min}}$	$\Delta_{T_{x,max}}$	$\Delta_{T_{x,min}}$	T_{max}	T_{min}
Jan550	8.88	-9.19	3.53	-2.96	78.52	-81.76
Jul550	7.82	-7.60	4.27	-2.84	72.10	-81.74
Jan500	8.94	-9.14	4.12	-2.90	79.09	-80.68
Jul500	7.54	-7.53	3.66	-2.83	72.66	-80.68
Jan450	9.42	-10.08	3.78	-2.86	79.71	-79.53
Jul450	7.59	-8.25	3.24	-2.79	73.28	-79.52
Jan400	9.39	-10.02	3.84	-2.78	80.35	-78.31
Jul400	8.17	-8.20	3.18	-2.70	73.99	-78.29
Jan350	9.82	-9.12	4.76	-2.73	81.10	-77.00
Jul350	8.34	-8.29	3.40	-2.68	74.70	-77.00
Extremes	9.82	-10.08	4.76	-2.96	81.10	-81.76

Table 3.8: Temperature gradients and temperature extremes [°C]

Table 3.8 shows positive and negative temperature gradients over time of ten °C per 15 seconds. Across the length of the tape spring, temperatures can vary up to five degrees Celsius over steps of 6 mm.

Temperature extremes are +81.1 °C and -81.8 °C. These temperatures are likely to occur for a wide variety of satellite orientations. The maximum expected temperatures in orbit would be when case 3 in Chapter 3.3 is applied. This would lead to maximum temperatures of just under 91 °C, shown in Figure 3.18. It is also observed from the graph that the base temperature of the tape spring is indeed lower than for cases 1 and 2, as the satellite body itself collects less heat due to its longitudinal axis being aligned with the sun vector. It should be noted that this worst-case orientation for the tape spring is unwanted and unlikely to occur, as this would also orient the satellite's solar cells away from the Sun.

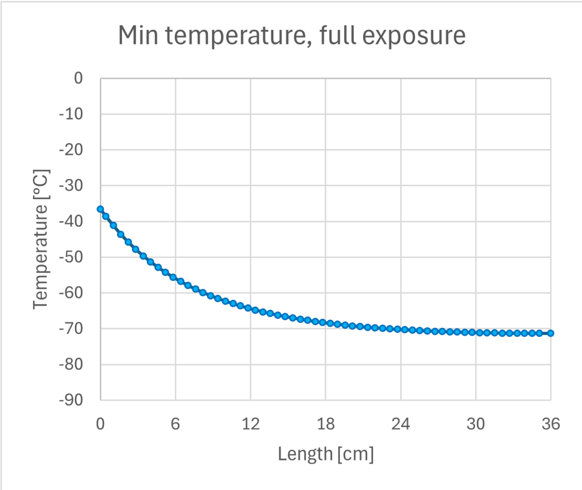

(a) Minimum temperature along the tape spring in eclipse

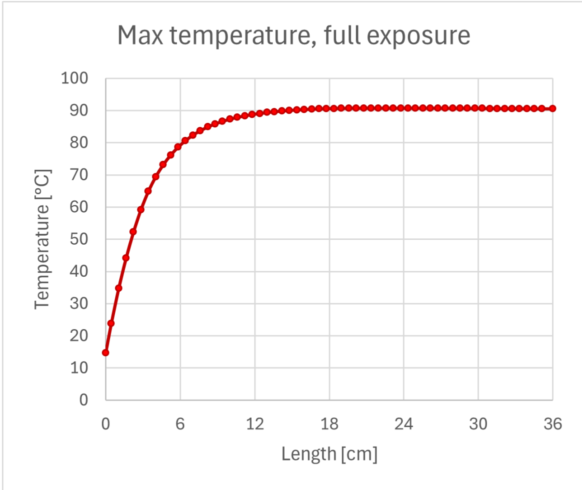

(b) Maximum temperature along the tape spring in sunlight

Figure 3.18: Worst case temperature extremes

3.7. Thermal model conclusions and discussion

Based on the ESATAN thermal model results, a shape memory alloy should be selected with an activation temperature no lower than 90 °C. This accounts for peak temperatures of 81 °C and any uncertainties in the model. An activation temperature of 100 °C may be desirable to account for incidental worst-case orientations, where the tape spring is facing directly towards the Sun for a full Sun-lit phase and reaches temperatures of up to 91 °C. It should be noted however that most of the satellite lifetime is spent above the lower altitude ranges where temperatures are at their highest, further lowering this risk.

High temperature gradients can lead to micro-cracks in composite materials due to resulting stresses. The rapid temperature cycling seen in these results can thus be an issue for the CFRP composites that are used. Han and Kim [8] ran thermal cycling tests between +100 °C to -70 °C in 2006 using halogen lamps, and found that this thermal cycling contributed significantly to a 4.4% loss of tensile stiffness in their material. The test was performed at a rate four times slower than the thermal cycling rate seen in the model results. Thus, it is not unreasonable to assume that a similar or higher loss of stiffness can be expected for the tape spring. As material stiffness is the driving force behind the neutral stability trait of the tape spring, this may require further testing.

4 Material Selection and Manufacturing Testing

The next step of the project is to verify that the method of Schultz et al [22] is viable for manufacturing. To this end, materials are selected and demonstrator springs are manufactured in the DASML composite lab at the faculty of Aerospace Engineering.

4.1. Selected Materials

4.1.1. Fiber

Schultz et al made use of a 85 grams per square meter (gsm) plain-weave T300 carbon fabric [22]. The best comparable fiber that could be found on the market is a 90 gsm variant provided by EasyComposites [4], which was selected for this experimentation. The layup used is the same symmetrical layup of two woven layers at ± 45 degrees angle used in the previous work. The properties of the fiber can be found at Torayca [16].

4.1.2. Resin

The results of the sensitivity study performed in Chapter 2.2.1 and the tests conducted by Schultz et al show that in order to create a neutrally stable tape spring via this method, a resin with a stiffness that is much lower than that of typical thermoset resins is needed. Based on the test results, a shear stiffness of no more than 0.2 GPa is preferred. According to Hyer [9], a typical stiffness range for epoxy resins is 1.1-2.2 GPa, which are stiffnesses that are well above this threshold for neutral stability.

All three resins used in the Schultz et al research (Table 2.1) are epoxy resins. Out of these three, only CTD-BG1.3 has a shear stiffness that is close to typical epoxy resins and both CTD-5XQ and CTD-10XQ are too stiff to achieve a neutrally stable tape spring. All three of the resins are no longer commercially available, and market analysis revealed no resins with a base stiffness close to required stiffness values. A resin with flexibilizing compounds is therefore required.

A solution was found in 2017 research performed by Callens and Bergsma [3] who studied the effects of supplementing the epoxy mix EPIKOTE EPH 04908 epoxy / EPIKURE EPR 04908 hardener, with EBL 1435, a flexibilizing epoxy matrix. The goal of this research was to lower the stiffness of the EPIKOTE matrix. The results of this research are summarized in figure 4.1, showing the decrease of stiffness with various percentages of added EBL 1435.

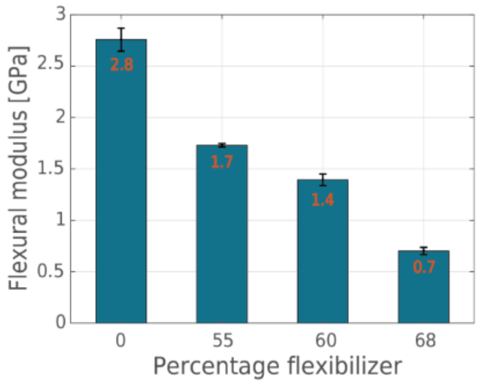

Figure 4.1: Flexural stiffness of EPIKOTE 04908 epoxy, with EBL 1435 added as a flexibilizer [3]

The decision was taken to use the blend with a 68 percent fraction of flexibilizer as an initial resin. This is based on the following:

1. EPIKOTE EPH 04908 and EPIKURE EPR 04908 are already freely available and in ample supply at the Aerospace faculty composites laboratory;
2. Most flexibilizer datasheets do not provide mixture properties beyond a percentage of roughly 30%. Such percentages typically do not lower the stiffness of resins to the stiffness levels required for this project;
3. In order to find the data for higher ratios of flexibilizer, mechanical testing would have to be conducted prior to manufacturing of the tape springs. Because this data is already available from the research of Callens and Bergsma, the testing step can be skipped by using the EPIKOTE/EBL blend.

Both the regular EPIKOTE/EPIKURE mix as well as the EBL modified blend were used in initial experimentation. The mixing ratio of the regular mix is 100:30 respectively, according to manufacturer specifications. The mixing ratio of the EBL modified blend is found using Equation 4.1. It is used by Callens and Bergsma [3] to find the required parts per hundred (PPH) of a resin using the epoxy equivalent weight (EEW) and amine equivalent weight (AEW) of two resins and a hardener, and their respective mass fractions:

$$PPH_{epikote} = 100 \cdot \frac{AEW_{epikure}}{M_{\%epikure} \cdot EEW_{epikure} + M_{\%EBL} \cdot EEW_{EBL}} \tag{4.1}$$

The equation yields a ratio in parts per hundred of 22.4:52.8:24.8 of EPIKURE, EBL and EPIKOTE respectively, using the values in Table 4.1.

Property	Short	Magnitude	Unit
Amine Equivalent Weight of Epikure	$AEW_{epikure}$	50	[g/mol]
Epoxy Equivalent Weight of Epikure	$EEW_{epikure}$	165	[g/mol]
Epoxy Equivalent Weight of EBL	EEW_{EBL}	251	[g/mol]
Mass Fraction of Epikure	$M_{\%epikure}$	0.32	[-]
Mass Fraction of EBL	$M_{\%EBL}$	0.68	[-]

Table 4.1: Mixing equation variables

A potential downside mentioned by Callens is the glass transition temperature of the resin blend, which lies between 37-57°C. This is below the operating temperature of the tape spring, and the matrix will thus cross the glass transition temperature. As a result, the matrix may become more rubbery and

Diameter	Pull force [g]	Recommended current [mA]
0.25 mm	930	1000
0.2 mm	590	610

Table 4.2: Properties of used SMA wires

flexible. This can potentially be beneficial to enhancing neutral stability. However, it remains to be seen if the spring makes a complete recovery to its original shape when cycled through the operating temperature range.

4.1.3. SMA

Schultz et al describe the use of an SMA wire with a diameter of 185 micrometers. Requirements for the wire that is to be selected are to roughly match this dimension and have an activation temperature of 90 degrees Celsius or higher, based on the results of the thermal modeling in Chapter 3.

The solution was found with the nickel-titanium wires of SmartWires [24], trade named Flexinol. These wires are available at activation temperatures of 70 °C and 90 °C, in diameters ranging from 0.5 microns to 500 microns, allowing great flexibility in wire selection. During the project, two of these wires were used with the properties shown in Table 4.2. Due to a later corrected error in the thermal modeling, the wires used in experiments were of the 70 °C variant.

4.2. Manufacturing Method

The initial tape springs are manufactured using the vacuum bagging technique. Schultz et al use a metal tube with a diameter of 1.25 in or 31.75 millimeters in their prototype tape spring design. This is reproduced as closely as possible: a metal tube with a diameter of approximately 32 mm is used as a profile for the layup, with a 21 millimeter diameter rod used later as an attempt to scale down the tape springs. The rod is secured to a long metal plate to facilitate vacuum bagging and its ends are sealed off with blue masking tape to prevent the vacuum bag from being sucked in to a vacuum space in the tube. This can potentially create a stress concentration and tear the bag and must be avoided. The layup is created by adding alternating layers of resin and carbon fiber. It is completed by successively adding a peel ply and breather layer to facilitate release. Breather fabric is applied across the full tube, covering off any sharp edges at the tube ends that could cause a leak. A breather path is created to a vacuum connector. The tape spring is then left to cure under vacuum for a minimum of 48 hours at room temperature, and is subsequently debagged and post-processed to its final dimensions. The tape spring then requires a drying period of between one and two weeks to achieve full cure and reach the final stiffness. The stiffness of the tape springs was observed to be lower with an incompletely cured matrix, making the springs more neutrally stable for this time.

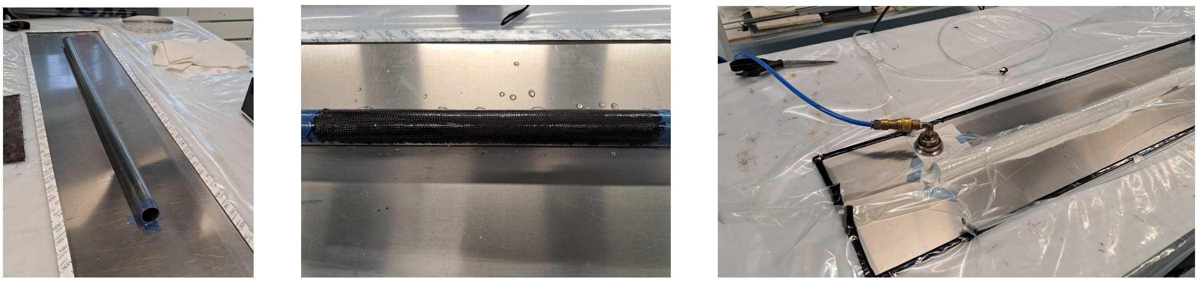

(a) (b) (c)

Figure 4.2: Impression of tape spring lamination process

Seven tape springs were manufactured in the trial phase of the project. The goal of this was to establish a manufacturing plan and to find suitable tape spring dimensions. The final manufacturing plan is described in Appendix A and is summarized in the flow diagram in Figure 4.3. It should be noted that the mentioned oven cure was only introduced for the final spring and springs 1-7 were cured at room temperature. The flow diagram represents this final manufacturing process including the oven cure.

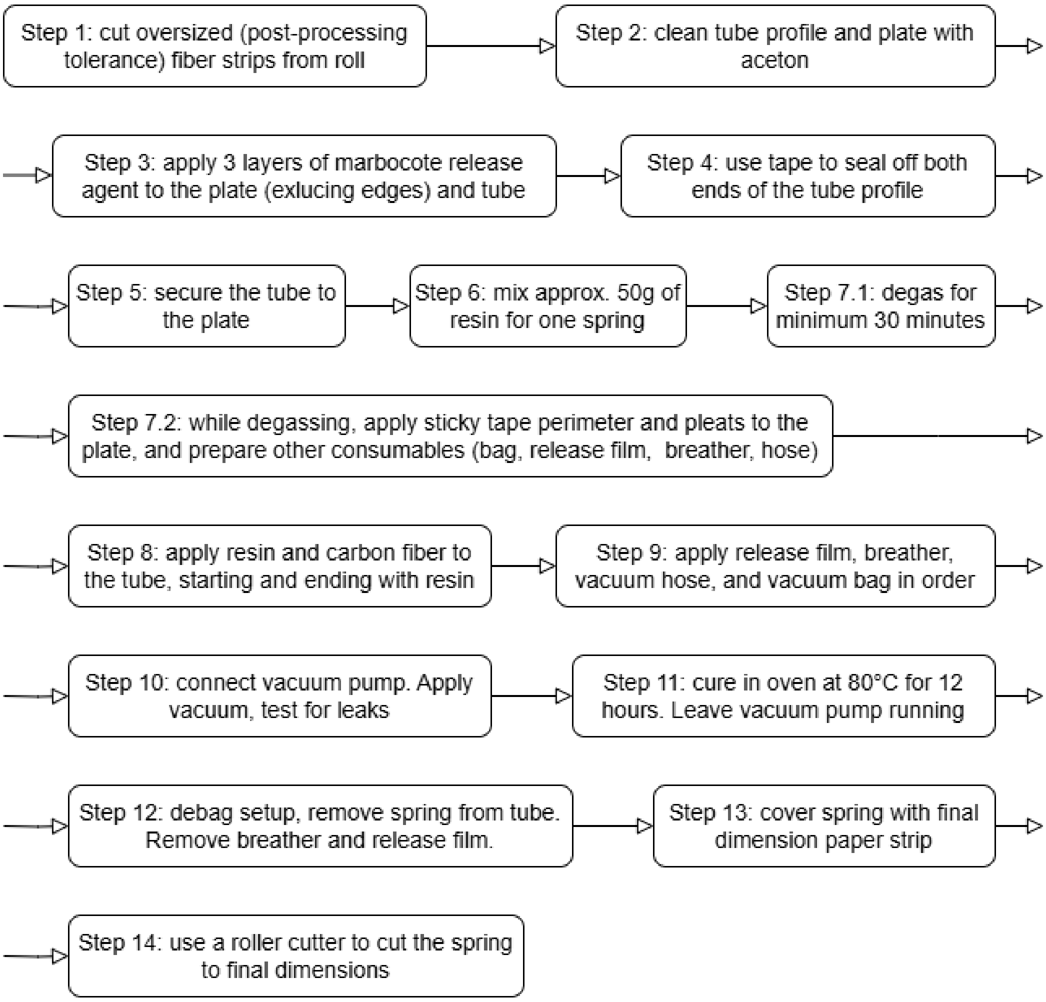

Figure 4.3: Summary diagram of the tape spring manufacturing process

4.3. Manufactured Springs

The springs that were built are discussed below. All springs were manufactured using a ± 45 or $[\pm 45]_S$ layup. Table 4.3 shows the properties of all springs that were manufactured in this stage of the project, as well as those of the eighth spring that was used for later testing.

Sample Nr.	Matrix	Tube diameter	Ply count	Spring length	Spanned angle θ
1	EPIKOTE+EPIKURE	32 mm	2	340 mm	180°
2	EPIKOTE+EPIKURE	32 mm	2	279 mm	138°
3	Callens blend	32 mm	2	279 mm	114°
4	Callens blend	21 mm	2	291 mm	83°
4.5	Callens blend	7 mm	2	320 mm	-
5	Callens blend	21 mm	4	360 mm	81°
6	Callens blend	32 mm	4	360 mm	111°
7	Callens blend	21 mm	2	360 mm	88°
8	Callens blend	32 mm	2	360 mm	80°

Table 4.3: Summary of manufacturing testing springs

4.3.1. Sample 1

First trial spring, built to test the initial manufacturing plan. The dimensions of this spring were not strictly controlled. The most important lesson learned from this first attempt is that the carbon fiber should not be pre-impregnated before being transferred to the tube. This leads to heavy warping which cannot be undone. The spring is visibly porous: resin is not completely filling the composite. This is a problem that was not solved during the project, despite attempts to add more resin and apply it more firmly. The low thickness of the fiber and low number of plies are possible factors.

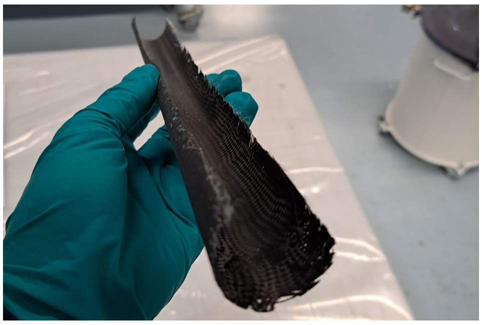

Figure 4.4: First sample tape spring

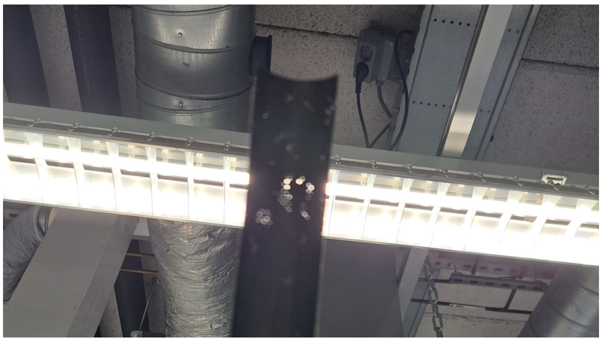

Figure 4.5: Porosity of two-ply springs

4.3.2. Sample 2

Second trial spring to test improvements to the manufacturing plan. The spring is shortened in order to make the fiber cutting process easier on the 100x30 cm roll that was still used at this point in the testing campaign. Some length is lost by applying a new layup technique: the dry fiber is secured to the tube using medium-temperature blue tape, after which resin is applied using a squeegee. The taped off part of the tape spring is not impregnated, remains dry and is removed after curing.

This spring was post-processed and does not have the rough edges seen in the first spring. Post-processing is done by using a paper inlay cut to the correct final dimensions, which is applied to the concave side of the spring and secured with tape. The excess carbon is then cut off using a pair of scissors. This can lead to sharp edges due to improper cutting.

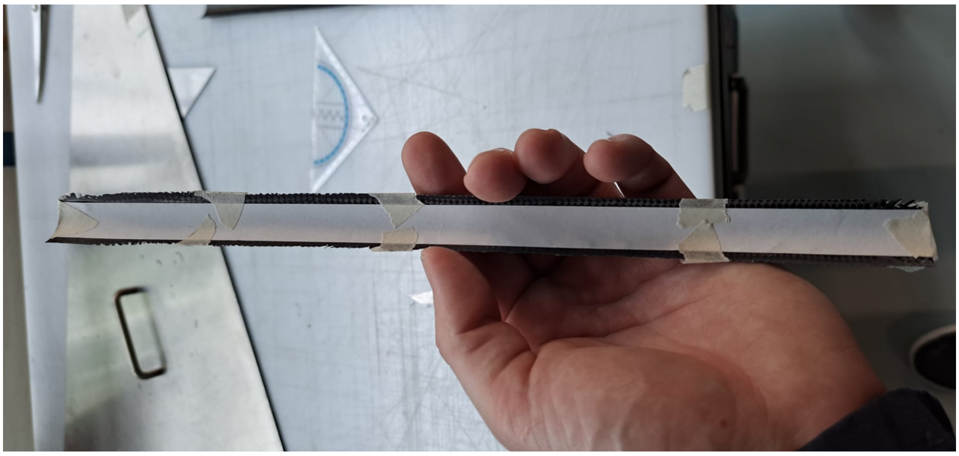

Figure 4.6: Paper inlay for post-processing

Due to numerous material defects, misalignments, and possibly stress induced by the scissor cutting process, there was a twist in the spring. This was observed by the spring not being level on the table. Both springs 1 and 2 were neutrally stable shortly after manufacturing, but this property diminished entirely several weeks later as the spring further dried, at which point the springs became bistable. It is thought that an impartial cure is responsible for this behavior: the matrix has a lower stiffness when it is not fully dried, leading to (partial) neutrally stable behavior. This then diminishes as the matrix dries and increases in stiffness.

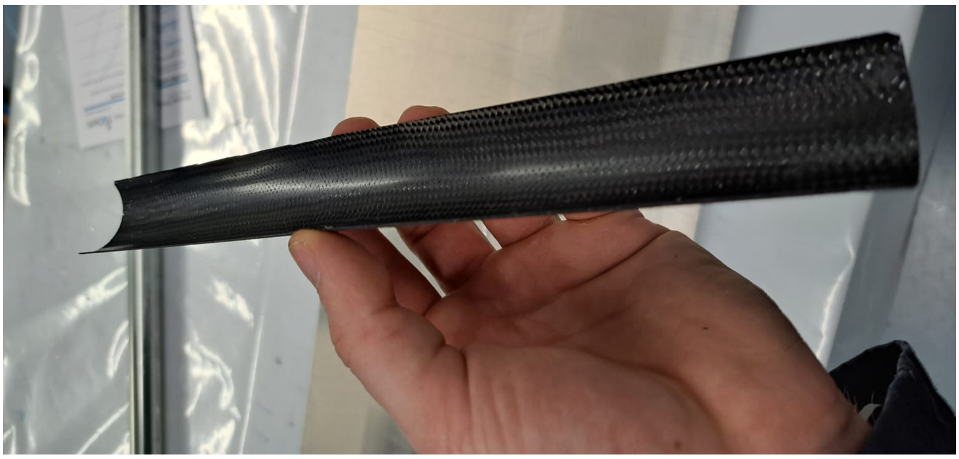

Figure 4.7: Second sample tape spring after post-processing

4.3.3. Sample 3
First spring to be made with the new resin blend discussed in chapter 4.1.2. The post-processing method changed to using a roller cutter instead of scissors to leave a smoother edge on the tape spring. The new resin drastically improved the neutral stability of the spring, which still partially diminished as the tape spring fully cured but never fully disappeared, even months later, at which point the spring was still stable at many points along its deployment path though not always fully neutrally stable. It is thought that the spring is on the limit between being bi-stable and neutrally stable.

This spring was also used to confirm a claim from Pellegrino and Miura [21] that the natural bending radius of a tape spring is equal to the diameter of the tool it is manufactured on. This was indeed confirmed: when the tape spring was rolled without applying any external forces to press the spring in to a smaller stored diameter, it would form a roll with an inner diameter equal to that of the 32 mm tube it was manufactured on. This is an important consideration for the sizing of a mechanism that is to make use of tape springs. While forcing the tape spring in to a smaller stored size is possible, this puts strain energy in the spring which is released when the tape spring is given room to expand, leading to an expansion involving shock that is ideally avoided.

4.3.4. Sample 4
Spring four scales down to a tube with a diameter of 21 mm and a smaller theta angle. The attempt was successful and the stability of the spring was not compromised. The smaller diameter tool leads to a tape spring with a smaller natural curvature radius, and the smaller theta angle reduces the force required to introduce a snap through in the tape spring, which is needed to enable rolling of the spring.

Figure 4.8: Springs three and four during layup demonstrating tape-down and folding technique

4.3.5. Sample 4.5
This spring was an attempt to scale down further and use a tube with a diameter of 7 mm. The attempt failed, as the carbon fiber cutouts repeatedly fell apart during manufacturing. A likely reason is the

narrow width of the cutout, which had a low number of tows across the width, leading to a low number of weaves and insufficient resulting friction to keep the cutout together when manipulated. The attempt was ultimately abandoned. It is possible that a cloth with more narrow tows and a more dense weave pattern may be better suited.

(a) (b)

Figure 4.9: Attempted 7 mm diameter tape spring

Failure to scale down the tape springs means that the ideal 7 mm size constraint provided by the Delfi team cannot currently be met with the tape spring mechanism. In order to create a tape spring of this size, the tape spring would have to be manufactured on a tool with a diameter of 6 mm or less, which does not yet account for any rolled-up antenna and SMA wire dimensions. Since it has proven to be impossible to lay fibers on such a scale by hand, it remains up to future efforts to scale down the tape spring to acceptable dimensions.

4.3.6. Samples 5 and 6

Springs five and six are the first springs made to the full length of 36 cm to accommodate the 36 cm antenna length set in the requirements, thanks to the purchase of a wider roll of carbon fiber. These springs are otherwise similar to springs three and four, but were made using four plies, with the goal of reducing the porosity seen in the previous tape springs (described in section 4.3.2). This defect was only marginally overcome, and resulted in the unwanted byproduct of significantly stiffening the tape spring, which increases the force needed for the snap through motion. This is expected to raise the actuation forces beyond what a feasible SMA component can overcome, and this path was therefore abandoned. The springs were largely neutrally stable and able to hold many points along the deployment path, but took more force to move from one position to the other.

A final change was made in the manufacturing plan, which is to lay the dry fiber by using a wooden stirring stick to gently drop the fiber on top of the base layer of resin. This leads to minimal disturbance of the fiber and resulting defects, as the fiber does not sag under its own weight as it is lifted on to the tool. Quality of the final product was further improved, and the tape-down and folding technique introduced for Sample 4 was abandoned.

4.3.7. Sample 7

Sample seven was made to 'round out the set' of having full length 36 cm springs on 21 mm and 32 mm tubes, in two and four ply variants. There are no new noteworthy conclusions from this sample.

4.3.8. Testing spring

At a later stage of the project, an eighth tape spring was manufactured made of two plies, Callens resin, and a length of 360 mm. A final modification was to oven cure this spring to skip over the one to two week waiting time for complete curing of matrix. This oven cure was performed at 80 °C for twelve hours. The spring was observed to be fully cured after the oven cure, eliminating the waiting time necessary for room temperature curing observed in all previous springs. This step was not used earlier as it was thought that the oven cure could make the tape spring brittle, which turned out to be false.

5
Design and Testing

5.1. Neutral tape spring design

As explained in Chapter 2.2, an external force is to be delivered by a wire made of shape memory alloy. The goal of this chapter is to estimate the actuation force that is required to supplement the internal strain energy to help overcome the internal friction of the tape spring, in order to achieve a deploying motion as the outcome of the sum of energies.

The actuation force for this concept actuator is provided by a shape memory alloy wire. When heated, the wire assumes a straight shape and shortens. When mounted in the lengthwise direction of the tape spring, this shortening generates a moment around the vertical centroid of the cross-section of the tape spring. The geometry involved is shown in Figures 5.1a and 5.1. The thickness of the spring t_{spring} was measured from the two-ply sample springs built in Chapter 4.3, the spring radius r is equal to the radius of the manufacturing tube and the vertical centroid $\overline{z}$ of the curved cross-section was determined via CAD software measurement to be 14.828mm. The length L is chosen in manufacturing and is set to 36 centimeters, which is the placeholder antenna length given for the Delfi project.

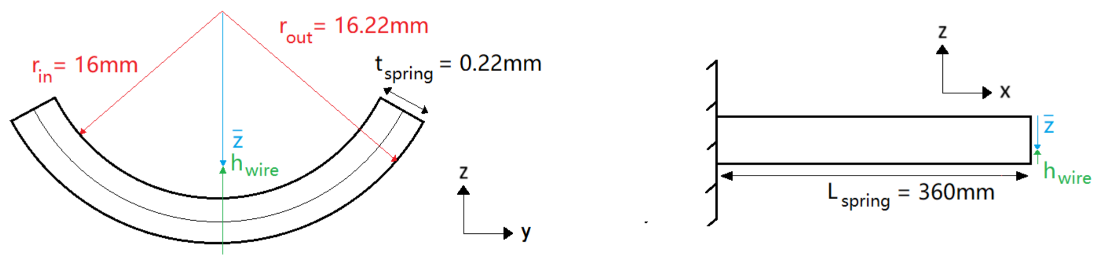

(a) Cross-sectional geometry

(b) Lengthwise geometry

Figure 5.1: Geometry of the unrolled tape spring

There are two variables in generating the actuating moment:

1. The force involved, which is generated by the SMA wire. This generated force is a function of the wire thickness: a thicker wire generates more force. Additionally, multiple of the same wire can be used in parallel to add more force, rather than simply using a thicker wire.
2. The moment arm, determined by the tape spring geometry and placement of the SMA wire.

There SMA can be mounted in two locations. The first option is to include the wire in the mid-plane of the laminate between the plies. The second option is to use a spacer on the tape spring that carries the SMA wire. The spacer is used to create vertical separation with respect to the vertical centroid in order to increase the moment arm for the SMA wire. The latter option was used by Schultz et al [22].

Compared to a spacer setup, a mid-plane wire is preferred, as this keeps the thickness of the total assembly consisting of the spring, wire and a possible spacer as small as possible. In the context of the Delfi project, where available space is very limited, a mid-plane wire setup saves many millimeters of space. The question is whether a mid-plane wire provides sufficient actuating force to move the tape spring.

In summary, the new energy balance in the spring is represented in Equation 5.1: the internal strain energy as well as the newly applied wire force drive deployment of the tape spring while still being counteracted by internal friction. The goal is to determine the required wire force needed to shift this balance to a positive value to enable the deployment of the tape spring.

$$E = E_{internal} + E_{wire} - E_{friction} \tag{5.1}$$

5.1.1. Mid-plane wire

Figure 2.1 has shown the three shapes a section of tape spring can take: unrolled (stress-free), rolled (stressed), or a transition zone between the two. When the spring is fully rolled, the cross-sectional geometry of the tape spring changes from the curved shape in Figure 5.1a to the flat shape shown in Figure 5.2. In this shape, the vertical centroid also moves to the mid-plane of the laminate. This means that an SMA wire in the mid-plane of the folded tape spring theoretically has no moment arm and cannot provide an actuating force. However, it is proposed that there are two reasons why this placement method can still work in practice:

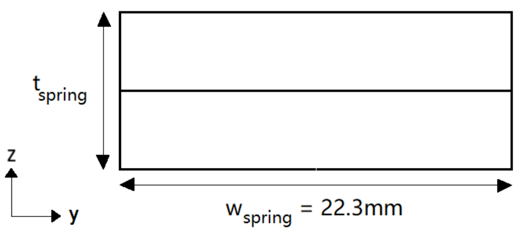

Figure 5.2: Cross-section of rolled-up tape spring

1. The SMA wire not only provides a purely contracting force because of its shape memory effect restoring strain, but also a moment from its shape change. When the tape spring is fully rolled up, the wire is coiled along with it. Activating the SMA wire forces the wire back in to its original straight line shape. This displacement 'drags' the tape spring along with it. This is not a length-wise compression that generates a moment using the vertical separation between geometric centroid and wire location, but a pure rotation around the Y-axis of the spring. This rotation force is difficult to quantify but does have an effect.
2. An increasingly larger section of the spring changes back into its unstressed, curved shape as the spring unfolds. In theory, this should provide an increasingly larger length of the SMA wire with a moment arm relative to the out-of-spring centroid shown in Figure 5.1a, generating an ever increasing moment as the spring unrolls. Figure 5.3 illustrates this concept. This may be sufficient to sustain a chain reaction that unrolls the tape spring.

This design has no moment arm and therefore serves as a benchmark test to demonstrate whether the above described hypotheses of shape change forces and moments and the possibility of a chain reaction due to cross-sectional shape change are true or false.
Besides the unknown rotation moment generated by the wire shape change, there are two more forces that are not quantified at this stage:

1. The internal friction of the tape spring. A method could not be found to estimate this friction within the time frame of this thesis. Thus, it is left out of scope.
2. The displacement force generated by the internal strain energy present in the tape spring, which is a function of curvature (spring dimensions) and material properties.

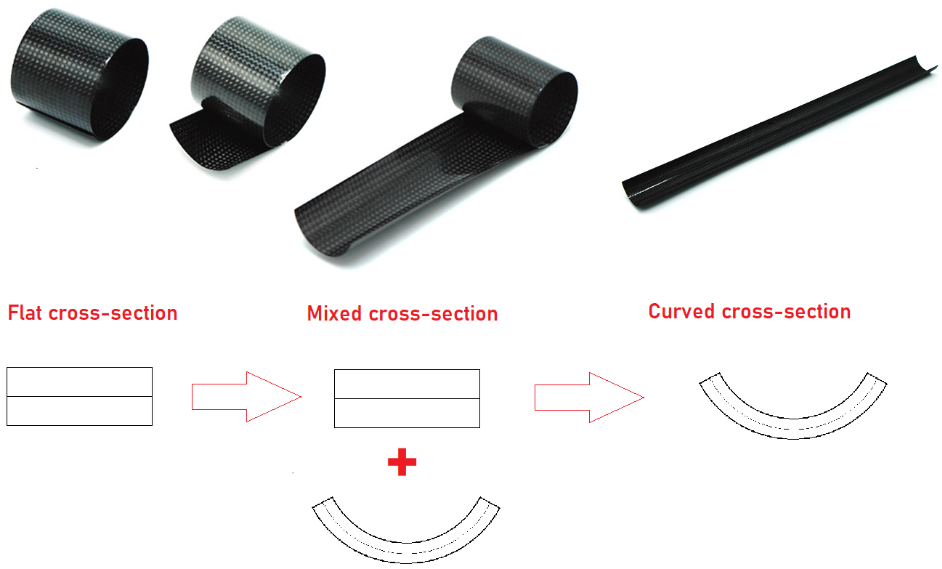

Figure 5.3: Change in cross-section during unrolling process

With the above two forces not quantified, it is difficult to predict the unrolling behavior of the tape spring. In order to make an estimate of the necessary wire force, it will be assumed that the spring is perfectly balanced in a neutrally stable state, such that the internal friction and internal strain energy due to compressed curvature are equal. This assumption is supported by the occasional observation of bi-stable behavior in manufactured tape springs as described in Chapter 4.3. In practice however, the two energies are not equal and internal friction is likely to be slightly greater than curvature strain energy, as evidenced by the observed neutral stability and lack of self-deployment in later manufactured springs. Consequently, any deflections calculated in the following design sections are theoretically slight overestimates of the actual displacement, as a portion of the wire energy is expended to overcome internal friction. The wire used for the test is the 0.25 mm diameter variant, delivering a force of 3.28 Newtons.

Functional testing

A test was carried out by manufacturing a tape spring with a 0.25 mm diameter SMA wire described in Chapter 4.1.3 in between its two woven carbon fiber plies with the Callens resin blend as the matrix material. The wire provides a force of 335 grams. The spring is shown in Figure 5.4. The SMA wire protrudes from the ends of the tape spring to allow for the placement of electrical connectors.

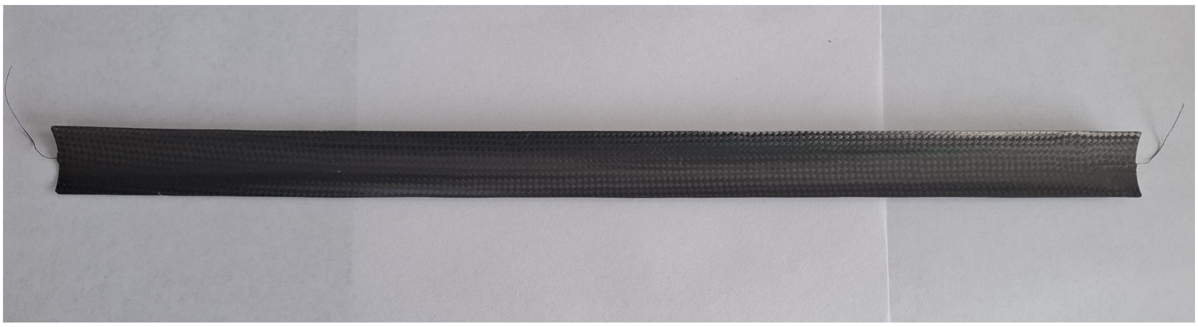

Figure 5.4: Neutrally stable tape spring with mid-plane integrated 0.25 mm diameter SMA wire

A 15V/10A lab power supply is used to power the SMA wire. The recommended current is specified by the manufacturer for each wire diameter and equals 1000 mA for the 0.25mm wire. The tape spring is rolled up as shown in Figure 5.5a and power is applied through the wire. To minimize the added mass that the mechanism must push, the tape spring is positioned on its side, with the clamp at the free end suspended above the test area, ensuring that added resistance from the clamp is minimal. Figure 5.5 shows the start and finish positions of the test, before and after the wire is charged and heated.

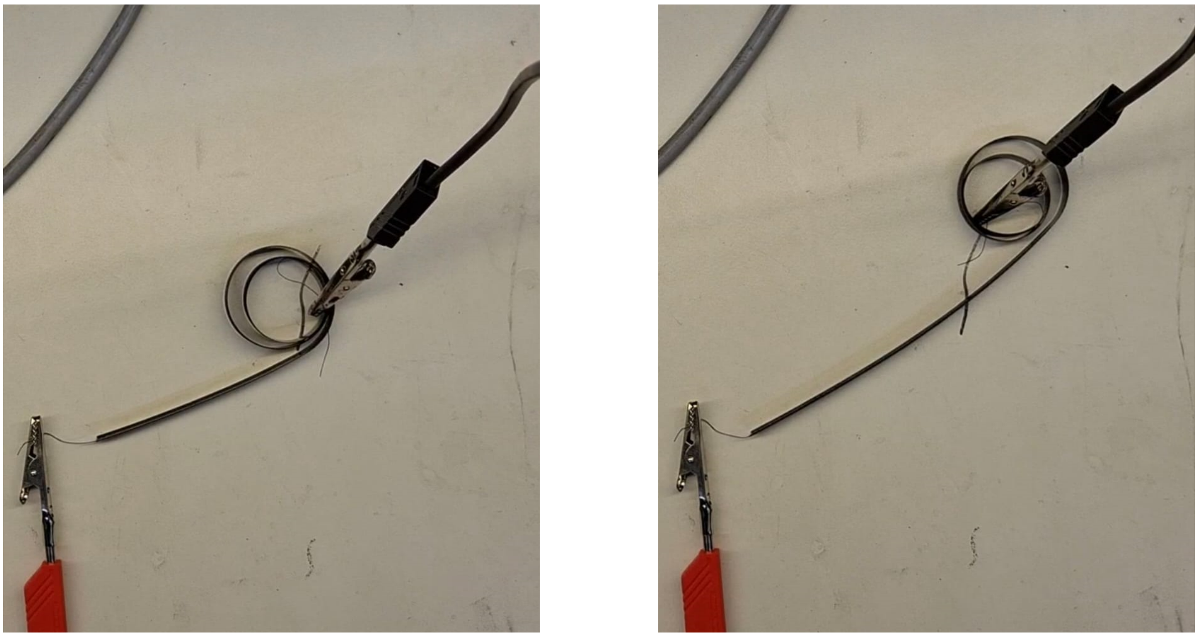

(a) Start position

(b) Finish position

Figure 5.5: Start and finish positions of the mid-plane wire tape spring

It is evident from the difference in start and finish positions that a considerable displacement has taken place of approximately 120 degrees, which is significant considering the fact that total deployment consists of a rotation of around 800 degrees. This is in contrast to the prior expectation that the SMA wire would be incapable of causing such movement due to a lack of any moment arm. The previous statement that the reshaping of the wire itself is also able to cause movement in the tape spring may be responsible for this behavior. This phenomenon is difficult to predict however, as the exact forces exerted here are not easily quantified.

It is further observed that the tape spring does not continue rolling indefinitely once rolling begins, as evidenced by its final position not reaching full deployment. Consequently, the hypothesis that partial deployment facilitates further deployment by providing a section of the wire with a moment arm relative to the geometric center as shown in Figure 5.3 appears to be disproven. A further key drawback of securing the wire inside the tape spring is that all generated heat is directly transferred to the tape spring. This makes the exceeding of the current tape spring matrix material's glass transition temperature a certainty.

This design may have more potential when combined with the four-ply tape springs manufactured in Chapter 4.3. The SMA wire could be embedded between two of the outermost plies, positioning it slightly away from the vertical centroid of the entire four-ply cross-section. However, this offset is expected to be negligible. Furthermore, given the significantly increased stiffness of the tape spring, the required SMA wire force is expected to be substantial, resulting in high power demands and increased heat deposition into the tape spring. For these reasons, such a test was not conducted and remains left open for possible future study.

5.1.2. Spaced wire

The main drawback of a mid-plane wire is the absence of a moment arm relative to the centroid of the tape spring's cross-section, which restricts its effectiveness to only that of possible moments generated by the shape memory effect. It is theorized that raising the wire further above the tape spring's cross-section could generate sufficient moment arm to enable the contraction of the wire to contribute to the bending motion. To this end, a spacer is introduced on top of the tape spring, similar to the work of Schultz et al. Since the wire is now positioned outside the composite, it is no longer co-cured and a fastening method is necessary to attach it to the tape spring. To help facilitate this, the spacer material is chosen to be double-sided tape with a thickness of 1 mm. The new flattened cross-section of the tape spring with added spacer is shown in Figure 5.6.

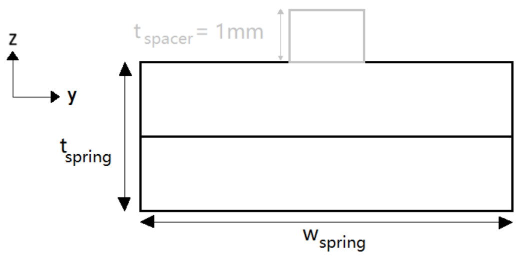

Figure 5.6: Updated Figure 5.2 cross-section with added spacer (not to scale)

To minimize additional material and mass, the tape is cut to the narrowest feasible width of approximately 5 mm and applied lengthwise along the tape spring. The SMA wire is encapsulated in a single layer of medium temperature tape to prevent it from melting through the double-sided tape before being attached to it.

Analytical design

A simple analytical design is performed to estimate the wire force required to sufficiently rotate the tape spring toward a full deployment for the various prototype actuators. Figure 5.7 shows the equation that is used.

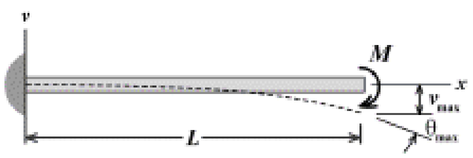

$$\theta_{max} = -\frac{ML}{EI}$$

Figure 5.7: Equation for the deflection of a cantilever beam loaded with a tip moment

While this equation does not exactly represent the bending scenario presented in the test setup, it is considered to be analogous, which is demonstrated in Figures 5.8-5.10. The curving effect of Figure 5.9 is applied in reverse: rather than curving the tape spring in to a spiral shape, the already spiral shaped tape spring is curved out to a flat tape spring. In this situation, the output curvature can physically go beyond 180 degrees, as the wire force remains parallel to the tape spring surface along the full tape spring length. This analysis serves only as an order of magnitude estimate, and it is understood that the cantilever beam deflection equation is not intended to be used for large deflections: the normal assumption of small deflections is neglected for this purpose, and it is expected that this method will have limited applicability.

Figure 5.8: Analogy between moment and force under an arm

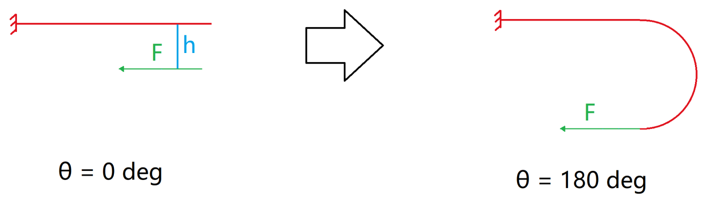

Figure 5.9: Curvature caused by offset force

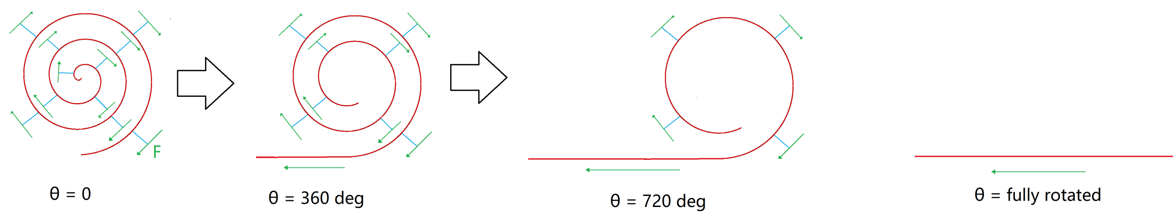

Figure 5.10: Reverse curving of the spring under constant parallel force

To find the output curvature of the wire force using the equation in Figure 5.7, the moment M, tape spring length L, tape spring stiffness E, and moment of inertia I of the cross-section in Figure 5.6 were found as shown in Table 5.1 as follows:

Property	Value
M	2.31$\cdot 10^{-3}$ Nm
L	0.36 m
E	2.492 GPa
I	1.543$\cdot 10^{-13}$ m^4

Table 5.1: Cantilever beam variables for the spaced wire tape spring

- E is found using classical laminate theory and the known material properties of the T300 fiber [16] and Callens resin blend (Chapter 4.1.2). A fiber volume fraction of 60%, fiber shear stiffness of 15 GPa, fiber Poisson's ratio of 0.2 and matrix Poisson's ratio of 0.36 are assumed;
- I is found by finding the second moment of area of the two individual rectangles constituting the cross-section as well as their combined centroid, followed by application of the parallel axis theorem to find the combined second moment of area;
- L is the tape spring length of 360 mm;
- Due to a shortage of the thicker 0.25 mm wire used in the mid-plane spring, a thinner variant of d = 0.2 mm was used as a substitute. M is found by multiplying the new wire force of 2.09 N by the distance between the wire and vertical centroid found during calculation of I.

The cantilever deflection equation yields an expected deflection of 171.56 degrees. While this is not enough to accomplish multiple rotations of the tape spring and reach full deployment, it is theorized that its combination with the moment caused by the shape memory effect which was observed in the mid-plane spring will yield a sufficient result.

Both of the following spacer wire tape spring tests make use of the eighth tape spring manufactured in Chapter 4.3.8.

Functional testing

A vise was introduced in order to clamp the tape spring and lift it off the table to further reduce friction. The new setup is shown in Figure 5.11. The free end clamp is again suspended to ease its movement by the tape spring.

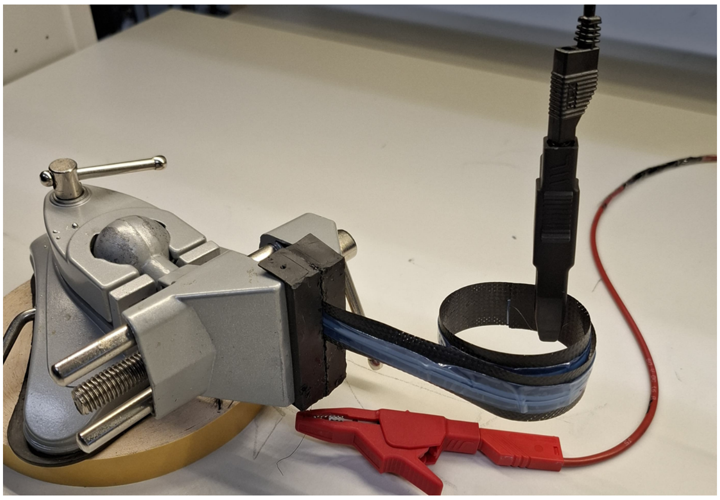

Figure 5.11: Spacer-enhanced tape spring setup

During setup, it was observed that applying double-sided tape to the straightened tape spring introduced tension in the double-sided tape when the spring was rolled. This tension caused the tape spring to unroll spontaneously similarly to the spring itself being bi-stable, and made it impossible for the tape spring to hold its stowed configuration. To partially mitigate this issue, the tape was reapplied while the spring was in a curved state, ensuring that the rolled configuration remained stress-free. This adjustment allowed the spring to better maintain its intended shape when rolled, but still lead to an increased diameter of the rolled spring. A minor drawback is that the spacer tape develops wrinkles when the tape spring unrolls, although this did not hinder its functionality. Figure 5.12 shows the difference made by this change.

(a) Stable rolled configuration when spacer tape is applied to a straight tape spring

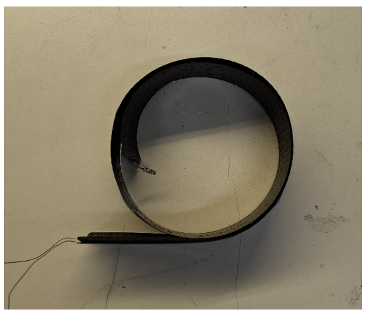

(b) Stable rolled configuration when spacer tape is applied to a curved tape spring

Figure 5.12: Difference in stable rolled configuration with the spacer tape applied to a straight or rolled tape spring

A manufacturer-specified current of 610 mA is applied through the wire. Figure 5.13 shows the start and finish positions of the experiment.

The displacement of the spring is shown to be considerably greater at approximately 580 degrees out of the maximum 800, despite this wire type providing less force than the one used for the mid-plane model tape spring. This appears to prove that even a small moment arm makes the wire significantly more effective. However, the tape spring still fails to fully unroll.

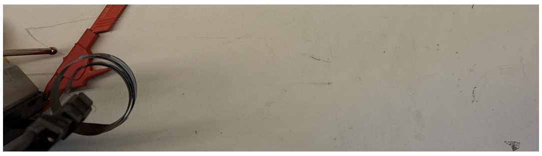

(a) Start position

(b) Finish position

Figure 5.13: Start and finish positions of the single-wire spacer setup

An observed downside to applying the spacer method is the impact of the added spacer material on the stiffness and curvature of the tape spring. With no external force to hold the tape spring in place, its diameter is increased, which may pose a problem concerning the volume constraints of the Delfi satellite.

The addition of the spacer separates the wire from the tape spring, preventing direct contact. As a result, the generated heat is mostly absorbed by the double-sided tape, allowing partial dissipation before reaching the tape spring. This alleviates some of the issues with excessive heating of the tape spring and exceeding of the glass transition temperature of the matrix material.

5.1.3. Parallel wires

The third and final tested actuating method involves the use of a pair of parallel SMA wires. This setup mirrors that of the spacer model, with the only modification being the addition of a second wire on top of the spacer. This configuration not only doubles the actuating force, but also establishes a return path for the electrical current to the clamped end of the tape spring. As a result, the electrical clamp is moved from the free end to the clamped end of the tape spring, ensuring that the test now remains entirely unaffected by the mass of the clamp.

Analytical design

The applied design method is identical to that of the single-wire spacer model, with the only modification being the doubling of the applied wire force, which increases from 5.79 Newtons to 11.58 Newtons with the addition of the second wire. The resulting output of the cantilever deflection equation also doubles to 343.12 degrees.

Functional testing

The previously described free end electrical clamp is relocated to the clamped end of the spring. The new setup is shown in Figure 5.14a.

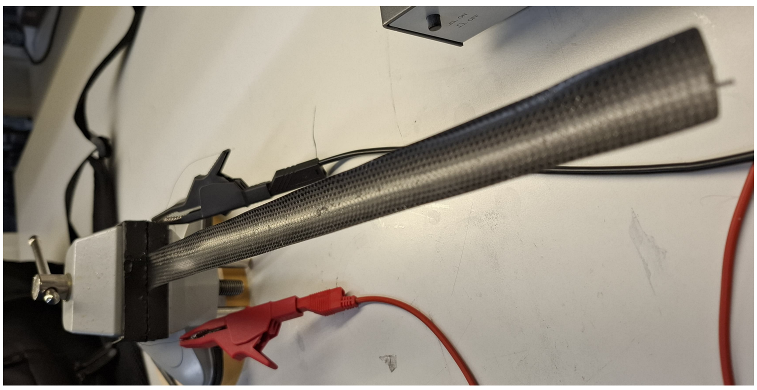

(a) Setup of the double wire tape spring

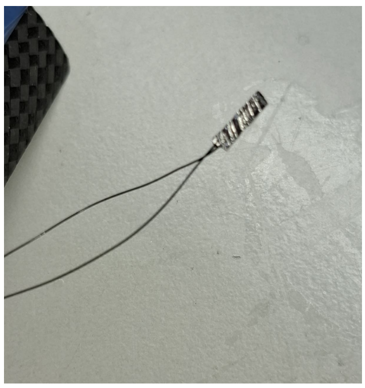

(b) Crimp connection

Figure 5.14: Double wire configuration

Due to the wire's tendency to straighten, a single wire cannot be used to create a back-and-forth path over the spacer, as this would introduce stress at the tip of the wire due to its inability to straighten out the return bend of the wire. Instead, the wire is cut into two sections and reattached in parallel at the free end of the tape spring. While soldering was initially considered for this connection, it was deemed unfeasible due to solder not adhering to the nickel-titanium material of the wire. Consequently, a crimp connection was adopted as a viable solution, shown in Figure 5.14b. This establishes an electrical connection between the two ends of SMA wire while adding minimal mass.

Power is applied to the wire and the tape spring is allowed to deploy. Figure 5.15 shows the start and finish positions of this test.

(a) Start position

(b) Finish position

Figure 5.15: Start and finish positions of spaced double wire test

The double-wire setup successfully achieves an almost complete deployment of the tape spring at roughly 700 degrees out of the maximum 800, with only a small 90-degree curvature remaining at the free end. The final stage of deployment of the tape spring is particularly challenging, as it requires an additional force input to induce a snap-through event to the fully straight configuration. However, the purchased SMA wires were unable to generate sufficient force to complete this transition. While full deployment is theoretically feasible, it is important to consider that if the ability to stow the tape spring is required via the use of an SMA wire in the opposite sense, then avoiding this final snap-through event may be beneficial. Reversing the snap-through motion is significantly more difficult using SMA wires. Therefore, it is advisable to leave the tape spring in the nearly fully deployed position achieved in this setup. Consequently, if a 36 cm antenna is to be deployed, the tape spring should be slightly longer than this length to ensure the full extension of the antenna without leaving its tip in a curved section.

It is important to note that the tape springs were not tested with a placeholder antenna wire. Similar to the addition of the spacer tape, the added stiffness of an antenna wire is expected to influence the rolling performance of the tape spring, potentially necessitating additional SMA material to provide more actuating force and achieve the same deployed position observed in the tests.

The analytical method provides a decent order-of-magnitude estimate of the necessary actuation force but a significant discrepancy remains. This is because the analytical model does not account for self-contact of the tape spring, resulting in friction, and the small-deflection assumption is violated. The described missing forces such as the internal strain energy of the not fully neutrally stable tape spring and other internal friction forces which were assumed to balance each other out to simplify the analysis are also missing, along with an estimation of the effect of the shape change moment that is caused by the shape memory effect and helps roll the tape spring. An FEM model is expected to provide a more accurate estimate for actuation forces, and such a model is recommended for increased accuracy.

6 Conclusions

This project aimed to study the feasibility of using a shape memory alloy wire for deploying a neutrally stable tape spring. It was conducted in three phases: thermal modeling, material selection, and tape spring testing. The key findings from each phase are outlined below.

Thermal modeling results indicate that the tape spring experiences temperatures ranging from a maximum of 81.1 °C to a minimum of -81.8 °C under most satellite orientations. In an extreme scenario where the tape spring's surface remains continuously exposed to the sun vector, the maximum temperature could reach 91 °C. However, this scenario was considered improbable for this project. Consequently, the minimum activation temperature for the shape memory alloy (SMA) component in the tape spring was set at 90 °C. Approximate temperature gradients were found during the thermal modeling. These are expected to have some effect on the stiffness of the tape spring, but have not been further studied.

An analysis of fiber types was left out of scope for the project. A variant was chosen based on the type used in previous research of Schultz et al. The T300 90gsm plain weave fiber was found to be suitable but posed manufacturing challenges, primarily porosity in most springs. This issue may be mitigated by using thicker fibers or additional plies; however, this would increase stiffness, making actuation with SMA wires more difficult, which is a drawback. A sensitivity study indicated that a stiffer fiber could result in a more neutrally stable tape spring, but this aspect was not further explored in the project. Both two-ply and four-ply tape springs were fabricated, with the latter expected to be too stiff for SMA wire actuation. The two-ply 80-degree span tape spring proved to be well suitable for testing and was able to deploy.

The Callens epoxy resin blend was chosen based on in-house test data, material availability, and its sufficiently low flexural modulus of 0.7 GPa, which enabled the fabrication of neutrally stable tape springs. The resulting springs were largely neutrally stable, though some exhibited minor signs of bi-stability. A key drawback of the Callens resin in this project is its low glass transition temperature, which is significantly below the tape spring's operating temperature. This may reduce stiffness of the tape spring, but also leads to somewhat permanent deformations of the spring which are best avoided. Given the availability of stiffness data from previous tests, the resin provided a good opportunity for an initial study of neutral stability in this thesis.

Scale-down experiments to reduce the tape spring diameter were performed during the project but were unsuccessful. As a result, the current tape springs remain too large to fit within the 7 mm design space allocated on the Delfi-Twin satellite by a considerable margin. However, springs with a diameter of 32 mm and 21 mm could be readily manufactured with some practice. With improvements to manufacturing techniques, it may still be possible to downscale to 7 mm.

Among the tested configurations—the mid-plane wire setup, spacer setup, and double-wire spacer setup—the double-wire spacer setup proved to be the most effective. The mid-plane wire model did

not perform well. Initially, it was hypothesized that restoring the curved cross-section during unrolling would provide the internal SMA wire with a moment arm, triggering a chain reaction that increased actuation power as the tape spring unrolls. However, this hypothesis appears to be disproven with the lack of a full deployment. In the mid-plane wire configuration, a moment arm is essentially absent because the vertical centroid of the flat cross-section coincides with the SMA wire's position. During testing, a small displacement in the tape spring was observed, possibly due to the shape memory effect of the SMA wire generating an additional out-of-plane rotational force that was not quantified. This effect needs to be further studied.
The single-wire spacer setup increased the deflection of the tape spring at the expense of increased dimensions, added mass, and added stiffness to the tape spring, causing the stored shape of the tape spring to further increase in diameter. This problem was successfully partially mitigated by applying the spacer material and eliminating tension in the rolled configuration. Additionally, the spacer provides the benefit of partial heat dissipation between the thermally activated SMA wire and the tape spring, which can help prevent the matrix material from exceeding its glass transition temperature.

The double-wire setup offers two key advantages: it increases the actuation force and provides a return path for the electrical connection, enabling both electrical connectors to be positioned at the clamped end of the tape spring. This design eliminates the need for an electrical connector at the free end, reducing the tip mass and simplifying deployment. The double-wire setup achieved a near-full deployment, proving the feasibility of the SMA actuated tape spring.

The simplified cantilever beam deflection analysis provided a starting point for required wires to test with, although there was a 200–400% discrepancy between the predicted and observed deflections. Therefore, a more precise model is needed for accurate deployment predictions and the creation of actuators with a high degree of precision.

The tape spring mechanisms have not yet been tested with an attached appendage, which is expected to increase stiffness and raise the required actuator force. However, given a thin enough antenna, it is expected that the added stiffness can be overcome by simply adding additional SMA to the tape spring to provide more force. Additionally, reversible deployment was not examined in this project. Achieving this would require training the SMA wire to match its memorized shape with the stowed shape of the tape spring, a process that demands precision at higher temperature which was not expected to be feasible to perform in-house at DASML. A possible solution may be to order a custom-made, pre-trained SMA wire from a manufacturer.

7 Recommendations

Several enhancements can be made to the thermal model. The optical properties of the satellite body, such as absorption and reflection, were estimated based on typical ranges for the surface materials used on the satellite and tape spring. However, physical measurements would provide more precise values. Similarly, the satellite's thermal capacity was treated as a variable to align with observed orbital temperature measurements from Delfi-Twin's predecessor, Delfi-PQ. This data shows some inconsistencies in thermal swing, likely due to rotations and tumbling motions around the velocity vector of the satellite, which cannot be accurately specified from the ground. A more precise definition of these motions would improve model accuracy.
Moreover, the conductive link between the satellite and the tape spring could not be precisely defined, as their exact connection has not yet been designed. Further study is required into the shape factor and material conductivities to specify the link. Additionally, previous research suggests that temperature gradients may influence the stiffness of the tape spring, an effect that must be accounted for in a flight model. Similarly, other spaceborne damage mechanisms, which were not addressed in this thesis, should also be considered for such a model.

It is recommended to select an alternative matrix material with a higher glass transition temperature. While this replacement can also have lower stiffness than the Callens resin, it is important to consider that some residual strain energy from material stiffness can be beneficial. This stored energy contributes to the deployment force, reducing the required force output from the SMA component. Achieving an optimal balance between inert stiffness and actuation force should be a leading design feature.

With continued practice, the manufacturing quality of the tape springs improved over time. However, further refinements are recommended, including the integration of automation techniques for fiber cutting and the potential use of prepreg materials to eliminate defects such as fiber misalignments in order to improve the consistency of the tape springs and possibly enable further downscaling to meet the 7mm size requirement.

With regard to the mid-plane wire variant of the tape spring, future studies could explore the possibility of fabricating four-ply tape springs and embedding the wire between two outer plies, which would create a slight moment arm relative to the vertical centroid of the cross-section. Further improvements to the spacer variant may be possible by selecting a non-isotropic spacer material that is stiff in the vertical direction to maintain separation between the SMA wire and tape spring while remaining less stiff along the tape spring's length to minimize tension buildup during rolling. However, no such material has been identified.

Besides the SMA actuation force, three other forces were not investigated in this project: the internal strain energy resulting from the flattened, normally curved cross-section of the deployed spring, the internal friction of the tape spring, and out-of-plane rotational forces induced by the shape memory effect of the wire. To accurately predict the rolling deflection of the tape spring, these forces should be quantified in a future study. A finite element method (FEM) model is considered a suitable solution, as it can account for self-contact of the tape spring and incorporate friction forces, which were not included in the current analysis. Reversible deployment and antenna actuation also remain to be tested in future studies.

References

[1] AzurSpace. *SPACE Solar Cells*. 2024. URL: https://www.azurspace.com/index.php/en/products/products-space/space-solar-cells (visited on 10/29/2024).

[2] J. Bouwmeester. "The Architecture of CubeSats and PocketQubes". Available at https://pure.tudelft.nl/ws/portalfiles/portal/96183067/2021_08_10_PhD_Thesis_Jasper_Bouwmeester.pdf. PhD thesis. Delft: Delft University of Technology, Sept. 2021.

[3] S.J.P. Callens and O.K. Bergsma. "Two-matrix composites: Carbon fiber micropultrusions embedded in flexible epoxy matrices". In: *Composites Part A: Applied Science and Manufacturing* 114 (2018), pp. 1–12. URL: http://resolver.tudelft.nl/uuid:b1a85c4f-cfc9-4253-9bcc-e3f1940dbc5d.

[4] EasyComposites. *90g ProFinish Plain Weave 1k Carbon Fibre Cloth*. 2024. URL: https://www.easycomposites.co.uk/90g-profinish-plain-weave-1k-carbon-fibre-cloth (visited on 05/24/2024).

[5] ESA. *How Hubble got its wings*. 2010. URL: https://www.esa.int/Enabling_Support/Space_Engineering_Technology/How_Hubble_got_its_wings (visited on 01/08/2024).

[6] N. Groeneweg. *MSc Thesis ESATAN Satellite Thermal Models*. 2025. DOI: 10.4121/f6299de4-2f65-4b3c-a573-00992e0819c1.

[7] M. Halvorson et al. "Advances in Bending Flat Plate Shape Memory Alloy Actuation Modeling Prediction of Actuation Behavior". In: *Proceedings of the 46th Aerospace Mechanisms Symposium*. 2022, pp. 61–74.

[8] J. Han and C. Kim. "Low earth orbit space environment simulation and its effects on graphite/epoxy composites". In: *Composite Structures* 72 (2006).

[9] M.W. Hyer. *Stress Analysis of Fiber-Reinforced Composite Materials*. Updated Edition. Lancaster, PA, United States: DEStech Publications, Inc., 2009. Chap. 3.

[10] K. Iqbal and S. Pellegrino. "Bi-stable composite shells". In: *41st Structures, Structural Dynamics, and Materials Conference and Exhibit*. 2000.

[11] D.C. Lagoudas. *Shape Memory Alloys: Modeling and Engineering Applications*. Boston MA, US: Springer US, 2008.

[12] J. Li et al. "Cyclic stress-strain characteristics of Ti-Ni and Ti-Ni-Cu shape memory alloys". In: *Materials Science and Engineering: A* 202 (1995).

[13] J. Mar and T. Garrett. "Mechanical design and dynamics of the Alouette spacecrafts". In: *Proceedings of the IEEE* 57 (6 1969).

[14] MatWeb. *Aluminum, Al*. 2024. URL: https://www.matweb.com/search/datasheet.aspx?bassnum=AMEAL00 (visited on 10/29/2024).

[15] MatWeb. *Epoxy/Carbon Fiber Composite*. 2024. URL: https://www.matweb.com/search/datasheet.aspx?matguid=39e40851fc164b6c9bda29d798bf3726 (visited on 10/29/2024).

[16] MatWeb. *T300 Technical Datasheet*. 2018. URL: https://www.toraycma.com/wp-content/uploads/T300-Technical-Data-Sheet-1.pdf (visited on 02/27/2025).

[17] T.W. Murphey and S. Pellegrino. "A Novel Actuated Composite Tape-Spring for Deployable Structures". In: *45th AIAA/ASME/ASCE/ASC Structures, Structural Dynamics Materials Conference*. 2004.

[18] NASA. *Deployable Composite Booms (DCB)*. 2020. URL: https://www.nasa.gov/centers-and-facilities/langley/deployable-composite-booms-dcb/ (visited on 02/15/2024).

[19] OrbitingNow. *DELFI-PQ/2022-002CU*. 2024. URL: https://orbit.ing-now.com/satellite/51074/2022-002cu/2022-002cu/ (visited on 10/29/2024).

[20] Niels van der Pas. *Lecture Notes of Spacecraft Thermal Design, TU Delft*. Apr. 2024.

[21] S. Pellegrino and K. Miur. *Forms and Concepts for Lightweight Structures*. Cambridge University Press, Mar. 2020.

[22] M.R. Schultz et al. “Neutrally stable behavior in fiber-reinforced composite tape springs”. In: *Composites Part A: Applied Science and Manufacturing* 39 (6 2008).

[23] M. Shahryarifard, M. Golzar, and G. Tibert. “Viscoelastic bistable tape spring behavior modeled by a two-dimensional system with rigid links, springs and dashpots”. In: *Composite Structures* 258 (2021).

[24] SmartWires. *Flexinol*. 2024. URL: `https://smartwires.eu/index.php?id_product=1&controller=product&id_lang=1` (visited on 02/28/2025).

[25] R. Stalmans, J. van Humbeeck, and L. Delaey. “Training and the two way memory effect in copper based shape memory alloys”. In: *Le Journal de Physique IV* 01 (C4 1991).

[26] B. Strnadel et al. “Cyclic stress-strain characteristics of Ti-Ni and Ti-Ni-Cu shape memory alloys”. In: *Materials Science and Engineering: A* 202 (1995).

[27] O.M.A. Taha et al. “Experimental study on two way shape memory effect training procedure for NiTiNOL shape memory alloy”. In: *ARPN Journal of Engineering and Applied Sciences* 10 (17 2015).

[28] TU Delft. *Delfi-PQ EPS*. 2024. URL: `https://delfispace.tudelft.nl/grafana/d/Delfi-PQ_EPS/eps?from=1642032000000&to=1704758399999&orgId=1` (visited on 08/23/2024).

[29] C. Underwood et al. “InflateSail de-orbit flight demonstration results and follow-on drag-sail applications”. In: *Acta Astronautica* 162 (2019).

[30] R.J.H. Wanhill and B. Ashok. *Shape Memory Alloys (SMAs) for Aerospace Applications*. Singapore: Springer, 2017, pp. 467–481.

A Manufacturing Plan

This appendix sets out the full manufacturing plan for a tape spring as summarized in Chapter 4.

A.1. Required items

The following materials and tools are required. Note that all materials used on the lay-up plate must withstand a minimum temperature of 80°C.

It is necessary to make a reservation in the DASML LabServant schedule for a composite workbench, vacuum pump, and oven.

Personal safety:

- Safety glasses
- Lab coat
- Latex gloves

Constituent materials:

- (90gsm T300) plain-weave carbon fabric
- 'Callens' resin blend, or the following components in a respective ratio of 24.8:52.8:22.4:
  - Resin: EPIKOTE EPH 04908
  - Resin: EBL 1435
  - Hardener: EPIKURE EPR 04908
- SMA wire, if included in the mid-plane

Chemicals:

- Aceton
- Marbocote release agent
- Simple white cloth (for chemical application)

Tools:

- Scissors
- Roller cutter
- Metal ruler, length >40 cm
- Degassing chamber
- Metal tube, d = 31.75 mm or as required (used as mold)
- Flat metal plate large enough to fit the tube with at least 10cm of clearance from the plate edges
- Vacuum pump with resin trap

- Coiled metal wire

Consumables (preparation included in manufacturing steps):

- Painter's tape
- Peel ply
- Breather cloth
- Plastic tubin
- Medium-temperature blue tape
- Sealant tape
- Vacuum bagging
- Mixing cup
- Mixing stick
- Hose clamp (for mixing stick)
- Resin squeegee
- Small patch of scotch-brite 3M metal wool (roughly 5x5 cm)
- Double-sided tape

A.2. Manufacturing steps

Step 1: cutting fiber

The fiber is cut over-sized to allow for post-processing of rough edges. This means that the material does not have to be cut to millimeter accuracy. This means that the fiber can be cut by hand. The carbon weave roll is unrolled on a cutting table. A ruler is placed at a 45 degree angle to cut $\pm 45°$ plies from the roll. A metal weight is placed on the ruler to apply pressure and keep the fiber in place to prevent shifting during cutting. A roller cutter is then used along the length of the ruler to cut the ply. Figure A.1 shows this process.

(a) Placement using a weight **(b)** Use of a roller cutter

Figure A.1: Fiber cutting by hand

Step 2: preparation of the plate and tube

The metal plate and tube used as a mold must be cleaned and prepared with a release agent. Aceton on a simple white cloth is used to clean the tube and plate of any residuals from previous manufacturing runs. If necessary, a scraper can be used first. After cleaning, three layers of marbocote release agent are applied to the plate and tube, with a drying time of five minutes between each layer. It is important not to cover 1-2 cm of the edges of the metal plate in marbocote, as this is where the vacuum sticky tape is later applied which should not release. It is advisable to use painter's tape to tape off the edges, so that no marbocote is (accidentally) applied to the edges of the plate.

When the last layer of marbocote has dried, the painter's tape is removed. The ends of the tube are closed off with several layers of medium-temperature blue tape as shown in Figure A.3a in order to

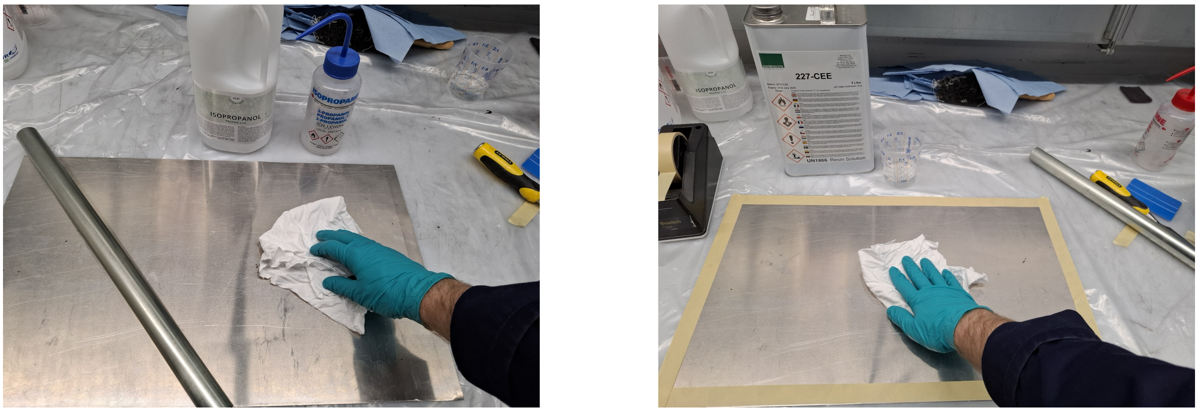

(a) Aceton cleaning using white cloth

(b) Marbocote application, taped off plate edges

Figure A.2: Chemical application

prevent vacuum suction in to the interior of the tube. The plate is then transferred to the composite workbench. The tube is secured to the plate with blue tape as shown in Figure A.3.

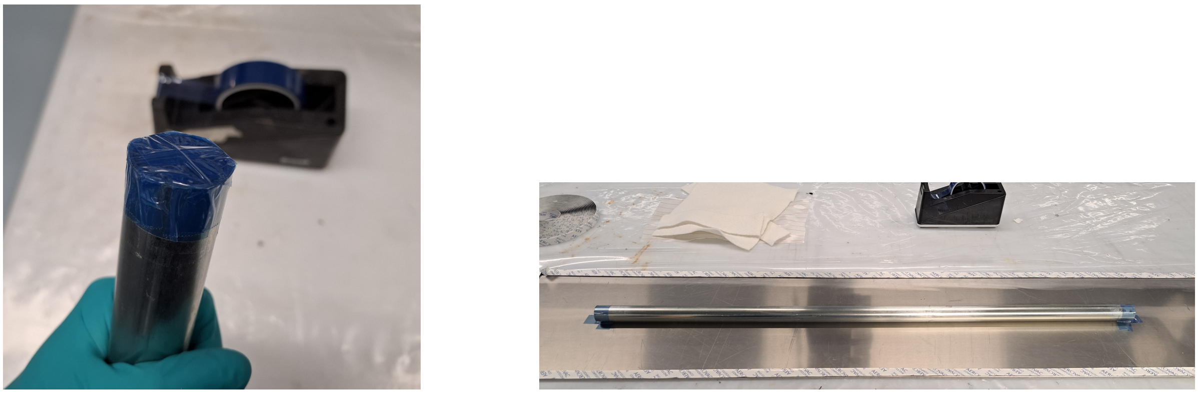

(a) Closed off tube end

(b) Tube secured to plate

Figure A.3: Setup of the baseplate and tube

Step 3: resin mixing
Resin is mixed in the chemical workbench, using the scale to achieve the ideal ratio of 24.8:52.8:22.4 parts of EPIKOTE, EBL and EPIKURE as closely as possible. It is advisable to combine resins in a large mixing cup, while pouring in resin components from smaller cups. Pouring resin directly from their containers makes the flow hard to control and easily leads to excess pouring. For a two-ply tape spring, 50 g - 70 g of total resin blend is recommended.

When the components are added to the mixing cup, they must be thoroughly mixed with a mixing stick. When completed, a piece of scotch-brite is added to the cup and secured to the bottom with the mixing stick and a hose clamp. This aids the degassing process. The cup is transferred to the degassing chamber, shown in Figure A.4b, and degassed for a minimum of half an hour.

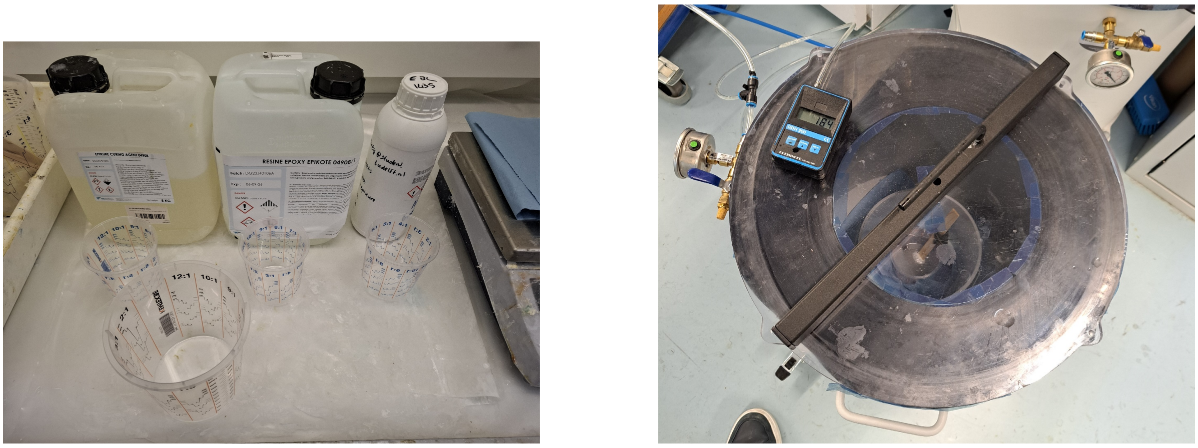

(a) Resins **(b)** Degassing chamber

Figure A.4: Resin making

Step 4: consumables preparation
While the resin is degassing the vacuum sealant tape is applied and the consumables for the layup are prepared. A ring of vacuum sealant tape is applied, followed by the application of pleats to facilitate stress-free suction of the vacuum bag around the product, shown in Figure A.5.

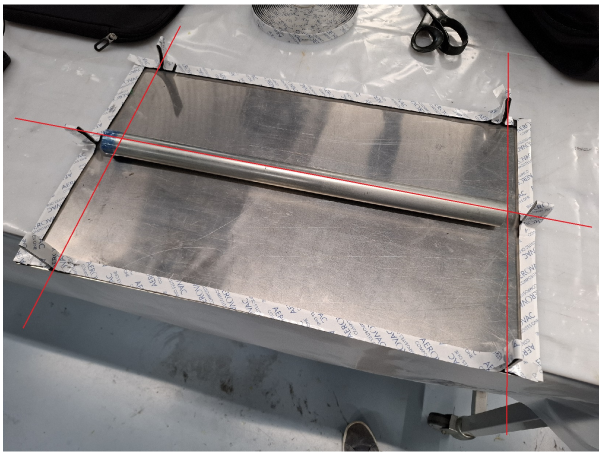

Figure A.5: Vacuum tape ring and pleats

Once the sealant tape is applied, the consumables for the layup can be cut. These are the vacuum bag, breather fabric and release plies. The vacuum bag should be the size of the plate plus approximately half a meter in each direction to account for the pleats and to have some extra margin. The breather fabric should be large enough to cover the tube and reach down to the plate. Some excess breather fabric is needed to create an air path from the tube to the vacuum connector. The peel ply should be of the same size as the fiber cut for the tape spring, plus a centimeter of margin at all edges of the spring. The vacuum hose should be long enough to reach from the inside of the oven to a vacuum pump outside. The vacuum hose should be internally filled with coiled metal wire so that the hose holds its shape when hot air is flowing through it and does not sag which can create a blockage.

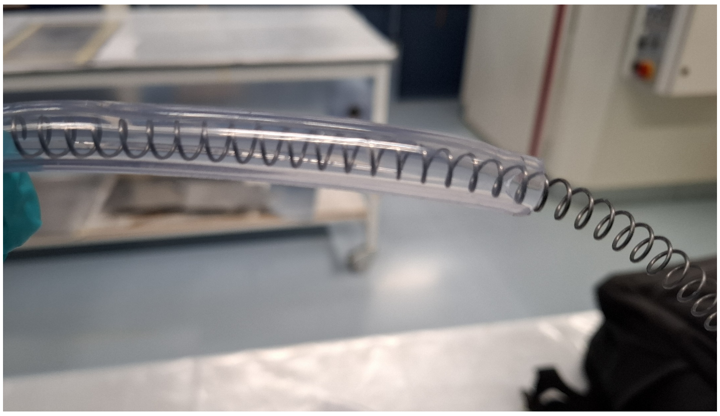

Figure A.6: Metal coiling used to support the vacuum tube

Step 5: lamination
Lamination is performed by applying alternating layers of resin and fiber, beginning and ending with resin. A mixing stick is used to transfer the fiber on to the tube in order to support its weight; if the fiber is transferred by hand, it will sag and stretch. This can be difficult to correct on the tube and should be prevented. A squeegee is used to apply the resin to the fiber.

Once the resin and plies are placed, the peel ply and breather fabric are added as shown in Figure A.7.

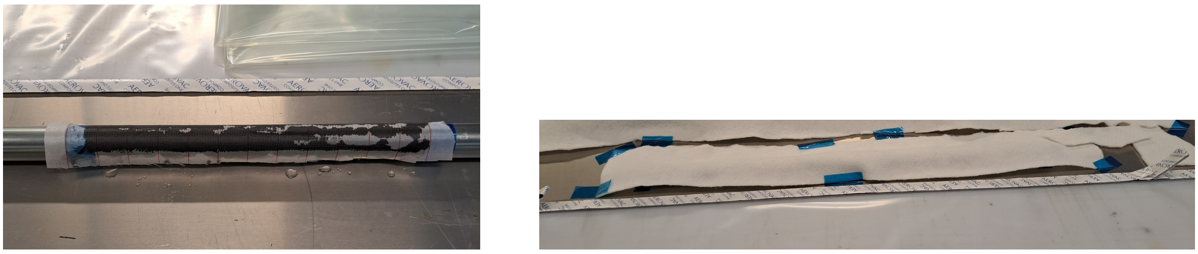

(a) Peel ply

(b) Breather fabric

Figure A.7: Fiber layering

Once the fiber and resin are laid, vacuum hose is placed at the end of the breather cloth path near the edge of the plate and secured with vacuum sealant tape. The product is then closed with a vacuum bag. The finished layup is shown in Figure A.8.

The completed layup is transferred to the oven and cured overnight at 80 °C for twelve hours.

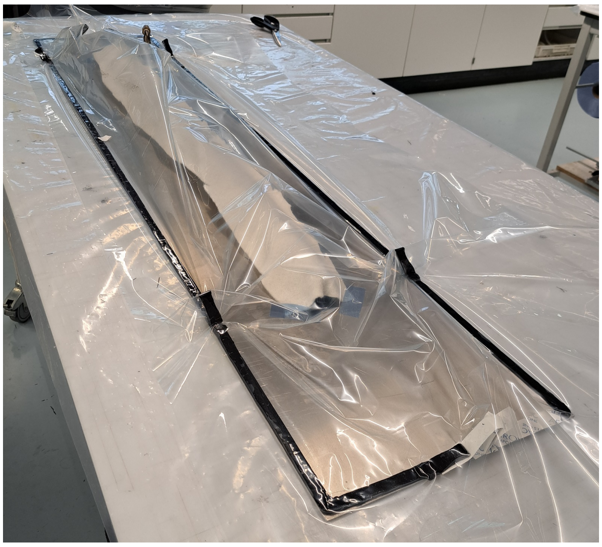

Figure A.8: Full layup

Step 6: post-processing
After curing, the plate is removed from the oven and all consumables can be removed. A Stanley knife may be needed to help in peeling off the peel ply from the carbon fiber.

The unprocessed tape spring is transferred to the fiber cutting workbench. Using an A3 sheet of paper, a paper strip of the final dimensions of the tape spring is created. This is laid in to the convex side of the tape spring and secured with painter's tape, as shown in Figure A.9. The tape spring is then secured to the workbench with double-sided tape and a roller cutter is then used to cut the tape spring to its final dimensions along the paper inlay. The paper inlay strip is then removed and the tape spring is completed. A very small section of the tape spring corners can be cut off if they are sharp.

Figure A.9: Paper inlay